JOURNAL OF GEOPHYSICAL RESEARCH, VOL. 96, NO. B10, PAGES 16,349–16,367, SEPTEMBER 10, 1991

Investigation of Deep Slab Structure Using Long-Period *S* Waves

JAMES B. GAHERTY[1]

Department of Geological Sciences, University of Michigan, Ann Arbor

THORNE LAY AND JOHN E. VIDALE[2]

Institute of Tectonics, Earth Sciences Board, University of California, Santa Cruz

Travel times and amplitudes of long-period *SH*, *ScSH*, *sSH*, and *sScSH* phases from several deep focus earthquakes in the northwest Pacific are analyzed for evidence of lithospheric slab penetration into the lower mantle. Inclusion of amplitude observations in the analysis provides constraints on lateral velocity gradients present in the deep slabs which are not resolvable using travel times alone. Travel time and amplitude residual spheres are presented for two deep focus events with good azimuthal coverage, but while interesting patterns are present, quantitative analysis is precluded by the lack of accurate methods for calculating synthetic long-period seismograms for three-dimensional slab models. Therefore, we focus our analysis on a two-dimensional approximation to the downdip geometry of the Kurile and Japan slabs, which allows comparison of a much larger data set with accurate two-dimensional synthetics, as well as the use of *sS* and *sScS* travel time and amplitude patterns as empirical corrections for deep mantle structure. While the limited azimuth range required for this approximation reduces the diagnostic capability of the data, it also increases our confidence that the corrected data are most sensitive to the near-source region. The *sS* and *sScS* observations indicate that the downdip shear wave travel time pattern previously attributed to a deep slab extension is primarily caused by broad-scale lower mantle heterogeneity. Once corrected for this structure, the *S* wave observations do not support a simple, undeformed slab steepening in dip and penetrating deep into the lower mantle beneath the Kurile and Japan Islands, as proposed by Jordan (1977) and Creager and Jordan (1984, 1986). Rather, the observations support shorter and/or broader slab models than those previously hypothesized: models which can probably be reconciled with *P* wave data. Further analysis of the complete three-dimensional patterns will be required for more precise resolution of the penetration depths of these slabs, if, indeed, any deep slab heterogeneity is actually seismically detectable.

Introduction

Determination of the structure and dynamics of subducting lithosphere is one of the foremost problems in Earth science. *Isacks et al.* [1968] first hypothesized that Wadati-Benioff zone earthquakes delineate cold lithospheric "slabs" that are sinking into the mantle at subduction zones. The magnitude of the thermally induced high seismic velocity anomalies associated with these slabs, the depth to which they penetrate, and the degree of deformation that they undergo en route, can potentially be determined by seismological analysis and used to place strong constraints on the nature of the upper mantle/lower mantle boundary and the style of convection present in the Earth's mantle. While some progress has been made in determining the properties of subducted lithosphere, proposed models of slab structure remain highly controversial, and thus the dynamic interpretations remain unresolved.

Perhaps the most fundamental question regarding slab structure is whether subducting lithospheric material penetrates into the lower mantle. Until the 1980s, seismological and geochemical observations were often interpreted as indicating that the subducted material is confined to the upper 650-700 km of the Earth. Seismicity in all Wadati-Benioff zones is observed to terminate at or above this depth range [*Isacks et al.*, 1968; *Isacks and Molnar*, 1971; *Stark and Frohlich*, 1985; *Rees and Okal*, 1987; *Frohlich*, 1989], and the deepest earthquakes in these zones have source mechanisms which generally indicate that the lithospheric slabs are in downdip compression at depths greater than 400 km [*Isacks and Molnar*, 1971; *Giardini and Woodhouse*, 1984; *Vassiliou*, 1984; *Apperson and Frohlich*, 1987]. When combined with the presence of a global 5-6% discontinuity in compressional and shear wave velocities at 650-700 km depth, these observations imply that subducting lithosphere encounters a contrast in material properties that resists deeper penetration.

The hypothesis that the change in material properties across the 670-km boundary is associated with, or accompanied by, a change in chemistry with sufficient density contrast to prevent the slabs from penetrating into the lower mantle is based on less direct evidence. One line of evidence is experimental work which indicates that the seismologically determined increase in density across the boundary is greater than that predicted for the expected phase changes to perovskite structure which take place near this depth for all of the common mantle minerals [e.g., *Jeanloz and Knittle*, 1989]. The notion of such a compositionally layered mantle is often invoked to provide multiple isolated reservoirs to account for chemical heterogeneity in mid-ocean ridge and ocean island basalts. Many researchers view the mineral physics experiments or seismological data as inconclusive, however, and favor interpretation of the 670-km discontinuity as entirely due to a phase change, perhaps associated with a viscosity increase that may cause mechanical resistance but will not prevent whole mantle convection (see *Silver et al.* [1988] for a review).

In the past few years, seismologists have been developing methods to image the velocity structure of the lower mantle

[1]Now at Department of Earth, Atmospheric, and Planetary Sciences, Massachusetts Institute of Technology, Cambridge.

[2]Now at U.S. Geological Survey, Menlo Park, California.

Paper number 91JB01483.
0148-0227/91/91JB-01483$05.00

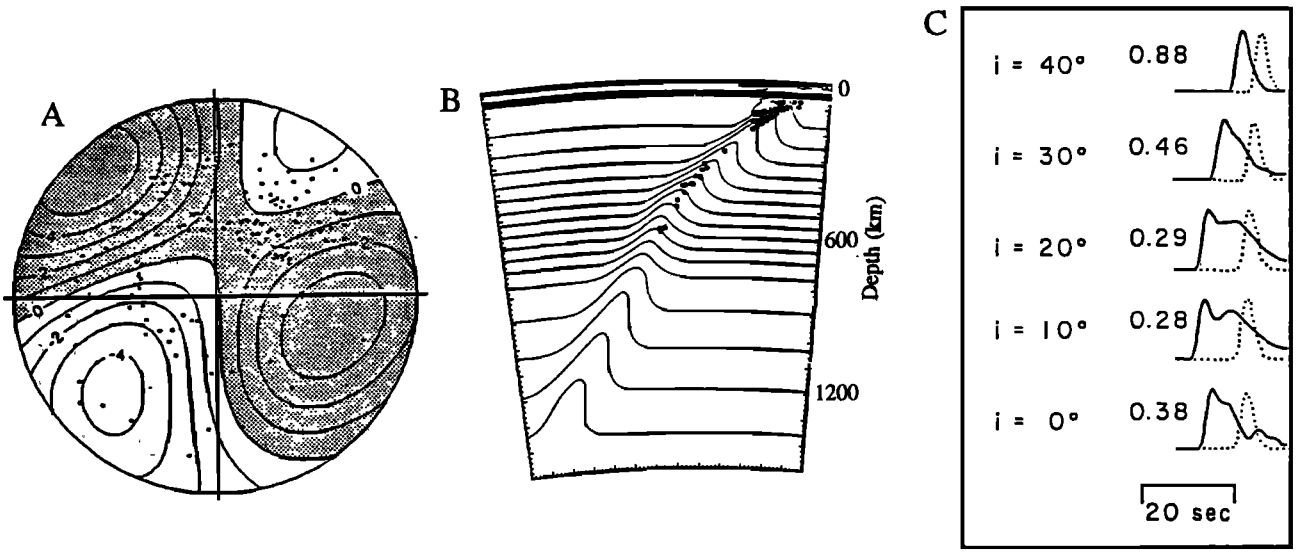

Fig. 1. (*a*) The smoothed *S* wave travel time residual sphere for event 8 analyzed by *Jordan* [1977]. Shaded areas are relatively slow arrivals, open areas are relatively fast arrivals, with contours in 1-s intervals. The strong NE-SW azimuthal trend, as well as travel time gradient in the NW quadrant, led to interpretation supporting deep slab structure. Figure is from *Creager and Jordan* [1984]. (*b*) Example slab model derived from *P* wave residual sphere analysis by *Fischer et al.* [1988], showing a high-velocity slab structure extending into the lower mantle with a steepening of dip below approximately 550 km. Velocity is contoured at 0.25 km/s intervals. (*c*) Synthetic *S* wave displacement pulses calculated for a model similar to to that shown in Figure 1*b* for a range of takeoff angles (*i*). Angle *i*=20° corresponds to the along slab-dip direction in the model. Numbers to the left of the pulse indicate the peak amplitude relative to PREM displacement (dotted pulses), and the extent of offset of the waveform relative to the PREM pulse corresponds to the travel time anomaly [*Vidale*, 1987].

beneath the deepest earthquakes. In general, the presence of a tabular high-velocity zone extending into the lower mantle can be used to argue (albeit not uniquely) for deep penetration of the slab, while lack of any such structure can be used to argue (also not uniquely) for deflection and containment of the slab in the upper mantle. Perhaps the strongest evidence favoring slab penetration below 700 km depth has been provided by several analyses of residual spheres for deep earthquakes [*Jordan*, 1977; *Creager and Jordan*, 1984, 1986; *Fischer et al.*, 1988, 1991]. The residual sphere [*Davies and McKenzie*, 1969] is a projection of travel time anomalies for a single event, corrected to the fullest degree possible for receiver and deep mantle anomalies, on a source focal sphere (Figure 1*a*). By comparing smoothed travel time residual patterns observed for individual deep focus earthquakes with synthetic residuals calculated for slab models with a variety of maximum penetration depths, these studies conclude that lithospheric material must penetrate with little distortion (other than steepening of dip and perhaps some advective thickening) to depths of at least 1000 km (Figure 1*b*) in many of the subduction zones in the western Pacific, including the Kurile and Japan slabs. However, several researchers [*Anderson*, 1987*a*; *Grand and Ding*, 1989; *Zhou and Anderson*, 1989; *Zhou et al.*, 1990] have recently argued that the residual sphere studies favoring deep slab penetration have failed to adequately account for the strength of near-source and/or deep mantle velocity anomalies. The latter studies assert that travel time residuals appropriately corrected for these anomalies cannot resolve or do not require lithospheric penetration into the lower mantle. This debate hinges on our knowledge of lower and upper mantle structure, which is very imprecise. Only when there is a much better understanding of the heterogeneous structure of the mantle as a whole will the complex residual sphere patterns be unambiguously explained.

In an alternate approach to this problem, several workers have directly inverted *P* and *S* wave travel time residuals from large sets of earthquakes for the velocity structure around and beneath Wadati-Benioff zone earthquakes. Tomographic images of the velocity structure of subduction zones in the northwest Pacific have been generated, with ambiguous results [*Kamiya et al.*, 1988, 1989; *Zhou and Clayton*, 1990]. While all of the studies resolve some features with intermittent high-velocity slab anomalies in the upper mantle, details of the structure in the uppermost lower mantle are poorly resolved. *Zhou and Clayton* [1990] conclude from these images that lithospheric slabs flatten to a subhorizontal orientation (beneath Japan) or spread outward at or near the 670-km discontinuity (beneath the Kuriles). *Kamiya et al.* [1988, 1989] conclude that the Japan slab steepens and penetrates into the lower mantle with a geometry similar to that preferred by *Creager and Jordan* [1986], while the northern Izu slab appears to bend horizontally westward near the upper mantle/lower mantle boundary. Attempts at resolution analysis [e.g. *Zhou*, 1988; *Zhou and Clayton*, 1990; *Spakman et al.*, 1989] are approximate and do not give great confidence in the noisy tomographic images. All of these studies utilize International Seismological Centre (ISC) travel time data, which have been shown to potentially be subject to systematic bias [e.g., *Grand*, 1990]; the conflicting conclusions drawn from similar data sets indicate that higher quality data will be required for resolution of this issue by tomographic methods.

Additional information on slab structure is contained within the waveforms and amplitudes of seismic body waves from deep earthquakes (Figure 1*c*). *Vidale* [1987] demonstrates that slablike velocity anomalies can defocus and severely distort synthetic waveforms with trajectories down the dip of the slab, and *Cormier and Kim* [1990] show that similar effects can be expected for ray paths within or at low angles to the slab, particularly along strike or obliquely downdip. *Suetsugu* [1989] analyzes short-period *P* wave travel time and amplitude observations from deep Kurile events and concludes that they are most consistent with a high-velocity slab penetrating below the 670-km discontinuity. In contrast, *Weber* [1990] compares amplitude (m_b) observations from the ISC catalogue with synthetic amplitude predictions and

concludes that the same Kurile slab does not penetrate beyond the 670-km discontinuity. *Silver and Chan* [1986] present complex waveforms recorded along the strike of the Kurile slab that they interpret to be due to multipathing along a lower mantle extension of the slab, although the multipathing interpretation has been questioned [*Cormier*, 1989; *Cormier and Kim*, 1990]. *Beck and Lay* [1986] analyze a similar, but more extensive, suite of data and conclude that the complexity observed by *Silver and Chan* [1986] is part of a broader pattern that may involve a deep slab extension but requires deep mantle heterogeneity as well.

In this paper, we attempt to constrain the deep structure of subducted slabs by jointly analyzing the travel time and amplitude behavior of a variety of horizontally polarized shear wave (*SH*) phases emanating from deep-focus earthquakes. Our primary sensitivity to deep slab structure is in the systematic behavior of *S* phases with respect to the slab. As mentioned above, *Grand and Ding* [1989], *Zhou and Anderson* [1989], and *Zhou et al.* [1990] contend that a substantial portion of the travel time variation observed by *Creager and Jordan* [1984, 1986] and *Fischer et al.* [1988] is due to long-wavelength lower mantle heterogeneity rather than slab extension into the upper part of the lower mantle. While the residual spheres analyzed by Creager and Jordan and Fischer et al. are corrected for lower mantle structure using model L02.56 of *Dziewonski* [1984] and smoothed to emphasize near-source variations, there is a strong concern that the heavily smoothed L02.56 model underestimates the strength of actual lower mantle anomalies, with the uncorrected lower mantle anomalies fortuitously projecting onto the residual sphere with a slablike pattern [*Zhou et al.*, 1990].

Given that existing lower mantle shear velocity heterogeneity models are of very low resolution, we use the upgoing ray paths, *sS* and *sScS*, to empirically correct for the deep mantle contribution to downgoing *S* and *ScS* paths. With these corrections, the resulting downgoing travel time residuals provide constraints on the velocity anomaly present immediately beneath the deep earthquakes, while the amplitude observations provide constraints on the deep velocity gradients. In this paper we primarily seek to understand the joint travel time and amplitude behavior of the seismic wave field in the downdip direction of the slab structure, making use of synthetic waveforms generated for this approximately two-dimensional geometry using the hybrid finite difference-Kirchhoff algorithm of *Stead and Helmberger* [1988]. We do not attempt to determine a single preferred structure for the Kurile and Japan slabs but instead evaluate the suite of slab models proposed by *Creager and Jordan* [1984, 1986] and *Fischer et al.* [1988] in terms of agreement with the *S* wave observations.

DATA ANALYSIS

We analyze over 760 seismograms from 25 intermediate and deep focus earthquakes from several northwest Pacific subduction zones (Figure 2 and Table 1); the seven best events are used for the evaluation of deep slab models, while all 25 are used to generate station statics. The data consist of long-period shear waves recorded globally on the World-Wide Standard Seismograph Network (WWSSN) and Canadian Seismograph Network (CSN), which we hand-digitized and rotated to obtain tangential and radial components. The events occurred between 1964 and 1984 and were selected on the basis of the following criteria: moderate size (m_b 5.5-6.1) with simple *SH* waveforms (indicative of minimal source complexity); favorable *SH* radiation to Europe and/or North America; and source locations resulting in dense station coverage at epicentral distances from 35° to 90° (thereby avoiding complexity in the waveforms due to upper mantle triplications or core diffraction).

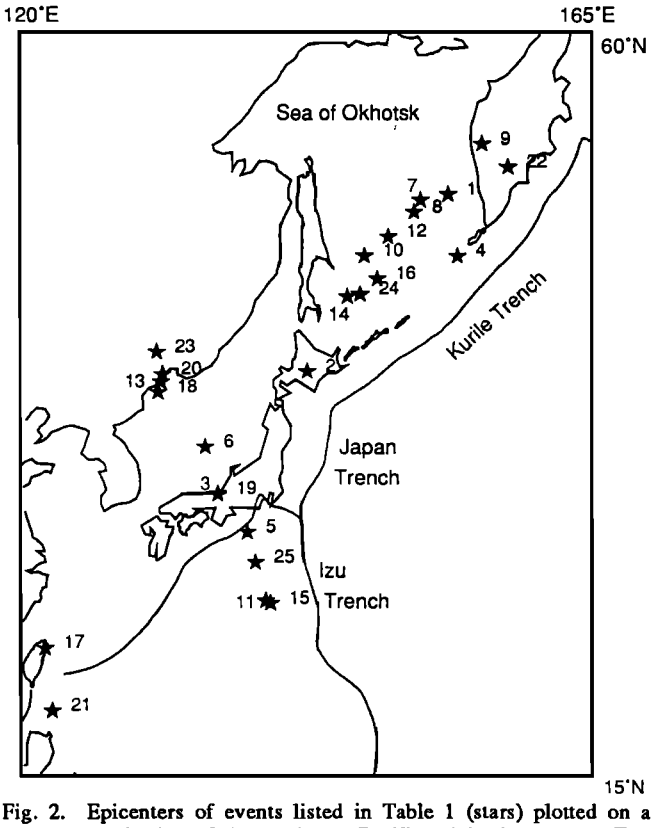

Fig. 2. Epicenters of events listed in Table 1 (stars) plotted on a Mercator projection of the northwest Pacific subduction zones. The majority of events are used to determine station correction factors.

Wherever possible, the long-period *SH* waveforms are analyzed over a time window that includes the phases *S*, *ScS*, *sS*, and *sScS*. We choose this suite of phases for a number of reasons. While the long-period waveforms are less sensitive than short-period energy to the narrow slab structures in which we are interested [*Weber*, 1990], they are also less vulnerable to rapid variations in attenuation and receiver structure known to complicate short-period amplitude observations [e.g., *Butler and Ruff*, 1980]. *SH* signals have relatively simple propagation effects away from the heterogeneous source region, including strong surface and core reflections and minimal receiver interactions, which facilitates the measurement of arrival times and amplitudes. Inclusion of the surface and core reflections ensures that the near-source region is sampled at a wide range of takeoff angles, which is critical for constraining the structure beneath the source.

For each arrival with sufficient signal-to-noise ratio, we measure a baseline-to-peak amplitude and a first-break arrival time, the latter having a conservative estimate of ±0.5 s relative accuracy. Travel time residuals are calculated using the predicted times for the ISC event location and origin time and the equivalent isotropic PREM 1-s shear velocity structure [*Dziewonski and Anderson*, 1981]; negative residuals correspond to early arrivals. Azimuth-independent *S* wave station corrections of *Toy* [1989] and *Wickens and Buchbinder* [1980] were applied. As discussed below, events are not relocated, as we ultimately restrict our attention to only a limited portion of the residual sphere. Amplitudes are equalized to an isotropic source by correcting for geometric spreading (calculated for the PREM model), the PREM attenuation structure, and double-couple focal mechanisms

TABLE 1. Event Information

Event	Date	ISC Location				Focal Mechanism			
		Origin Time, UT	latitude,°N	longitude,°E	depth,km	φ	δ	λ	References*
1	March 18, 1964	0437:25.7	52.56	153.67	424	48	84	-76	L83
2	July 4, 1967	2342:12.9	43.10	142.58	157	94	79	89	IM71
3	Aug. 13, 1967	2006:52.3	35.43	135.49	367	238	68	-84	ts
4	Dec. 1, 1967	1357:03.4	49.45	154.40	144	50	87	109	L83
5	Feb. 28, 1968	1208:01.8	32.95	137.85	348	180	86	97	M71
6	March 31, 1969	1925:27.0	38.49	134.52	397	38	75	230	ts
7	Sept. 5, 1970	0752:27.2	52.28	151.49	560	3	72	-90	ts
8	Jan. 29, 1971	2158:03.2	51.69	150.97	515	34	72	-110	ts
9	May 27, 1972	0406:49.6	54.97	156.33	397	24	85	-94	ts
10	Aug. 21, 1972	0623:48.6	49.47	147.08	573	15	17	47	ts
11	Jan. 31, 1973	2055:54.2	28.22	139.30	508	317	72	-74	ts
12	July 28, 1973	2006:35.4	50.45	148.92	585	51	76	-107	L83
13	Sept. 10, 1973	0743:32.3	42.48	131.05	552	24	17	107	ts
14	July 10, 1976	1137:14.0	47.31	145.75	402	41	89	-87	ts
15	Dec. 12, 1976	0108:51.1	28.04	139.67	503	328	72	-74	ts
16	June 21, 1978	1110:38.7	48.27	148.66	380	288	32	32	ts
17	Sept. 2, 1978	0157:34.2	24.81	121.87	115	34	28	138	ts
18	Aug. 16, 1979	2131:24.9	41.85	130.86	566	56	24	133	ts
19	March 31, 1980	0732:32.4	35.49	135.52	362	214	44	-149	ts
20	Nov. 27, 1981	1721:44.3	42.93	131.19	525	66	25	175	CMT
21	July 3, 1983	0249:28.2	20.19	122.41	221	332	37	-83	CMT
22	July 24, 1983	2307:31.8	53.91	158.36	190	319	1	4	ts
23	Oct. 8, 1983	0745:26.3	44.21	130.74	551	349	29	88	ts
24	April 23, 1984	2140:34.2	47.44	146.73	399	18	40	110	ts
25	April 24, 1984	0411:28.5	30.89	138.48	398	86	36	-150	ts

Focal mechanism is defined by the strike, dip, and rake of one of the nodal planes, in degrees, with the conventions described by *Aki and Richards* [1980].

*Focal mechanism references: L83, *Lay* [1983]; IM71, *Isacks and Molnar* [1971]; M71, *Mikumo* [1971]; CMT, Harvard CMT catalogue; ts, this study.

determined using the methodology described below. Amplitude station corrections are also calculated (as described below) and applied to the observations. The corrected travel time residuals and the logarithm (base 10) of the corrected amplitudes comprise the data set for the analysis.

Focal Mechanism Determination

To optimize the radiation pattern corrections, we employ a damped iterative least squares inversion technique to find the double-couple focal mechanism most consistent with the long-period *S* wave energy. *SH* and *ScSH* amplitude observations (corrected for attenuation and geometric spreading) are combined with *SH/SV* amplitude ratios and iteratively inverted for perturbations to the strike, dip, and rake of published *P* wave first motion or other starting mechanisms. Inversions resulting in a deviation from the initial mechanism of greater than 10° in any of the fault parameters are considered unstable, and the initial mechanism was retained. This only occurs for a few relatively sparsely recorded events. For a few well-sampled events, one of the three fault parameters is tightly constrained by polarity reversals, so that parameter is held fixed while the remaining parameters are determined. Our final double-couple mechanisms are included in Table 1.

As an example, Figure 3*a* depicts the lower hemisphere projection of the final solution for event 7, which had an initial mechanism with strike = 9°, dip = 74°, and rake = -85° [*Strelitz*, 1975], and a final mechanism of strike = 3°, dip = 72°, and rake = -90°. The corresponding reduction in variance of the amplitudes is 17%. For all 25 events, all of the observed *S*, *ScS*, *sS*, and *sScS* polarities are in agreement with the final mechanisms, justifying the use of double couple rather than more general moment tensor representations of these deep sources. We avoid using observations near radiation nodes since these have large correction factors.

Station Corrections

Prior to examining travel time and amplitude observations for near-source structure, effects of near-station crustal and upper mantle structure must be removed. Although station statics for S wave travel times have been calculated and interpreted by many researchers [e.g., *Sengupta*, 1975; *Wickens and Buchbinder*, 1980; *Romanowicz and Cara*, 1980; *Toy*, 1989], *S* wave amplitude statics have not been extensively studied for global data sets. Therefore, we apply a least squares inversion procedure to empirically determine the station statics for our amplitude data. In this procedure, for each of the 25 events, the *S*, *ScS*, *sS*, and *sScS* subsets (each corrected for *Q*, geometric spreading, and radiation pattern) are each considered as a separate "pseudoevent"; that is, the different phases for the 25 events give a total of 87 "pseudoevents" (some events lack *sS* and/or *sScS* observations). Event amplification factors are then calculated and removed from each pseudoevent using a least squares inversion that minimizes the scatter in the relative amplitude observations at each station. The mean value at each station is used as a station factor, with the overall set of station anomalies being normalized.

The results of this procedure are plotted in a lower hemisphere projection in Figure 3b. All 105 station anomalies are plotted at the direct *S* ray path position for the event 7 source location. In this projection, North American stations are in the northeast quadrant, European and Middle Eastern stations are to the northwest and west, and Asian, Australian, and Pacific island stations are to the south. Note the strong azimuthal pattern shifting from small arrivals at approximately N60°E to larger arrivals at N45°E. This pattern was previously observed by *Lay*

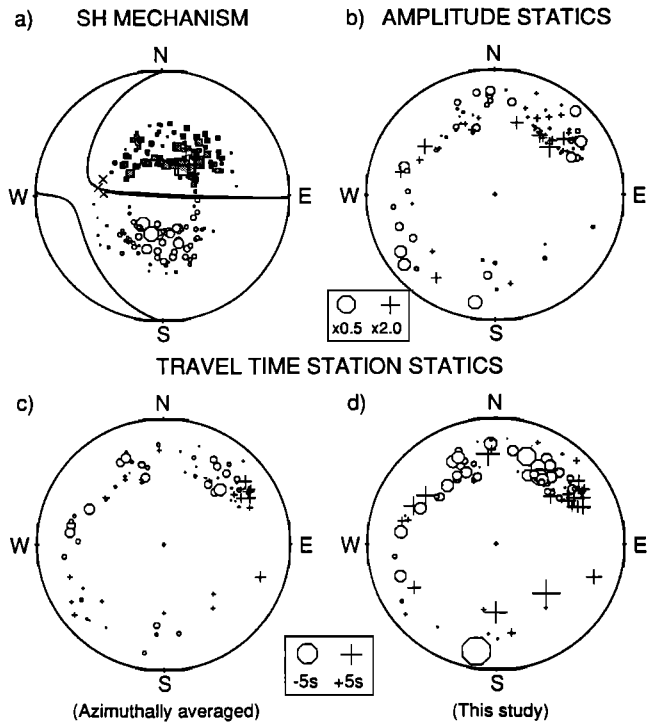

Fig. 3. Lower hemisphere projections of amplitude and travel time data using the hypocenter of event 7: (*a*) *SH* (*S*, *ScS*, *sS*, and *sScS*) amplitude observations from event 7, corrected only for geometric spreading and PREM attenuation structure, plotted with the final *SH* mechanism for the event. *sS* and *sScS* observations are projected to the lower hemisphere by correcting azimuth and takeoff angle by 180°. The azimuthal amplitude variation due to focal mechanism is clear. Crosses indicate nodal observations, and outer circumference corresponds to takeoff angle of 90°. (*b*) Empirical amplitude statics for all 105 stations, calculated as described in the text, and plotted at the *S* takeoff angle. Crosses are larger than average, and circles are smaller than average, with the size of the symbol indicating relative scale. Outer circumference corresponds to 60° takeoff angle. (*c*) Azimuthally averaged travel time statics for all stations (plotted at the *S* takeoff angle) from *Wickens and Buchbinder* [1980] and *Toy* [1989]. Crosses are relatively slow stations, and circles are relatively fast, with size variation indicating the relative scale. (*d*) Travel time statics for all stations determined empirically as described in text. Symbols are the same as those used in Figure 3*c*, and the circumferences of both Figures 3*c* and 3*d* correspond to takeoff angle of 60°.

and Helmberger [1983*a*], and is most simply interpreted as a change in the attenuation structure of the upper mantle, from low Q beneath the western United States to high Q beneath the eastern United States and Canada. Across Europe, the station statics vary rapidly, probably influenced by both attenuation and focusing variations, while the Australia and Pacific stations appear to have lower amplitudes on average.

An obvious hazard in empirically determining the station statics from this data set is the possibility of mapping systematic near-source structure to the receivers due to the similarity of the source locations within a group of westward dipping subducting slabs. We have attempted to minimize this by including sources from a variety of subduction zones with varying strike and dip (see Figure 2). In addition, by including observations spanning the full range of takeoff angles covered by *S*, *ScS*, *sS*, and *sScS*, we have ensured that a large subset of the data samples the near-source region at large angles to the strike and dip of the subducting slabs, and the greatest consistency in the amplitude anomalies should be due to the portions of the paths common to all phases, i.e., the near-station crust and upper mantle.

For the travel time station corrections, we have applied the azimuthally averaged statics of *Toy* [1989] and *Wickens and Buchbinder* [1980] (Figure 3*c*). These statics provide extensive coverage of the WWSSN and CSN networks, and the worldwide distribution of sources used in their determination ensures that the resultant statics are truly due to localized receiver mantle and crustal origins. However, it is known that receivers can exhibit strong azimuthal patterns [e.g., *Dziewonski and Anderson*, 1983]. To establish the influence of any azimuthal stations terms affecting our data, we also calculated travel time station statics from our data set in a manner identical to the procedure described above for the amplitude anomalies (Figure 3*d*). The empirically calculated residuals appear to be stronger (i.e., larger absolute value) than Toy's and Wickens and Buchbinder's, perhaps due to the lack of averaging over a variety of source locations. Overall, however, the correlation is reasonably high, with a linear correlation coefficient of 0.61, and the signal from the upper mantle structural variation across North America is again obvious, with the region beneath the western United States being slower than that beneath the eastern United States and Canada. The largest discrepancy between the azimuthally averaged residuals and ours appears to be at stations in the eastern United States and Canada, where our residuals are faster than the averaged values. This is consistent with the fact that South American sources give late arrivals for these stations [*Lay*, 1983], resulting in slower azimuthally averaged values relative to statics calculated for sources in the northwest Pacific. It is enticing to interpret our faster station residuals as due to long paths in a fast, deep root beneath cratonic North America [e.g., *Grand*, 1987] and therefore appropriate for correcting northwest Pacific-to-North America paths for receiver mantle structure. These paths roughly coincide with the strikes of the slabs being investigated, however, and we are concerned that all four phases (*S*, *ScS*, *sS*, and *sScS*) used to determine the station residuals may contain substantial near-source signal due to this geometry. Correction for these residuals could remove evidence of the near-source structure in which we are investigating, and we therefore take a conservative approach and use the published azimuthally averaged statics for our corrections. *Schwartz et al.* [1991] explore the observations in North America in greater detail. Note that our station residuals are very similar to Toy's at downdip azimuths where most of our analysis takes place, so the choice of station corrections does not critically influence our results.

RESIDUAL SPHERE ANALYSIS

The corrected travel time and amplitude observations can now be analyzed for patterns attributable to near-source and deep mantle structure. The residual sphere methodology allows for examination of both azimuthal and ray parameter patterns in the travel time and amplitude residuals. Note, however, that we have not attempted to remove bias in the travel time residuals due to potential source mislocation. While *Creager and Jordan* [1984, 1986] discuss the necessity of relocating the events used to analyze the *P* wave residual spheres, *Jordan* [1977] points out that any significant bias due to epicentral mislocation should be apparent on the residual sphere as a systematic variation in residual with the cosine of the azimuth (i.e., with a degree 1 pattern). In all well-sampled travel time residual spheres presented here, no such variation is observed. Errors in source depth primarily cause ray parameter-dependent trends; for example, if steeper rays are systematically relatively fast (as they consistently are in the data presented below), the source depth

may be underestimated. A vertically dipping fast slab may produce a similar ray parameter trend (accompanied by a degree 2 pattern), and thus this trend taken alone is fundamentally ambiguous. In every case that we observe a strong ray parameter trend in the downgoing phases, however, we observe a similar trend in the upgoing surface-reflected data that is opposite to that expected due to underestimation of the source depth. Thus, any attempt to eliminate the ray parameter trend in the downgoing data by shifting the source to a deeper depth will only enhance the upgoing trend, and vice versa. The balanced behavior between the upgoing and downgoing trends argues strongly against a significant depth mislocation in either direction. In addition, depth errors of over 80 km are required to account for the 2-3 s ray parameter trends observed in both the upgoing and downgoing data, which is much larger than the depth shifts found by relocating *P* waves. We conclude that an error in source depth is not responsible for the ray parameter trend, and any mislocation error that is present leads to travel time errors that are very small relative to our observed ray parameter trends, typically well under 0.5 s. While, in general, quantitatively relocating well-sampled events to remove systematic bias is not a difficult problem, such a procedure is unstable for uneven or sparse coverage of the focal sphere. Since most of our events have restricted or unbalanced azimuthal station distribution, we forego the relocation procedure and proceed with the requirement that azimuthal and ray parameter variations be interpreted cautiously.

Figure 4 presents travel time and log(amplitude) residual spheres for two deep Kurile events. The residuals are plotted on a lower hemisphere projection, with the center corresponding to a vertical takeoff angle, and the circumference corresponding to a takeoff angle of 60°. The travel time residual sphere for the January 29, 1971, event (event 8) is directly comparable to the residual sphere that *Jordan* [1977] determined for the same event using short-period *S* waves. *Creager and Jordan* [1984] show that source relocation has a very minor effect on the *S* wave residual sphere for this event, due to the lack of a degree 1 pattern (see Figure 1). Both travel time projections can also be compared with *P* wave residual spheres for these events determined by *Creager and Jordan* [1984, 1986]. The travel time patterns are dominated by the early arrival times at azimuths northeast and southwest from the source, which is along the slab strike direction (marked by arrows in Figure 4). *Jordan* [1977] shows that a high-velocity slab extending vertically beneath the event(s) can explain much of the pattern. In addition, the northwest quadrants of the travel time residual spheres are dominated by a strong trend with takeoff angle, with the *S* observations (outer band of observations on the figures) being 2-3 s slower than the *ScS* observations to the same stations. This is also consistent with the observations of *Jordan* [1977] for event 8, and can be explained by the same vertically extending high-velocity slab. The agreement between our travel time residuals and those determined from short-period data is encouraging, for it indicates that the decreased time resolution for long-period waveforms is offset by the stability of the waveforms, allowing for compensating consistency in the travel time picks.

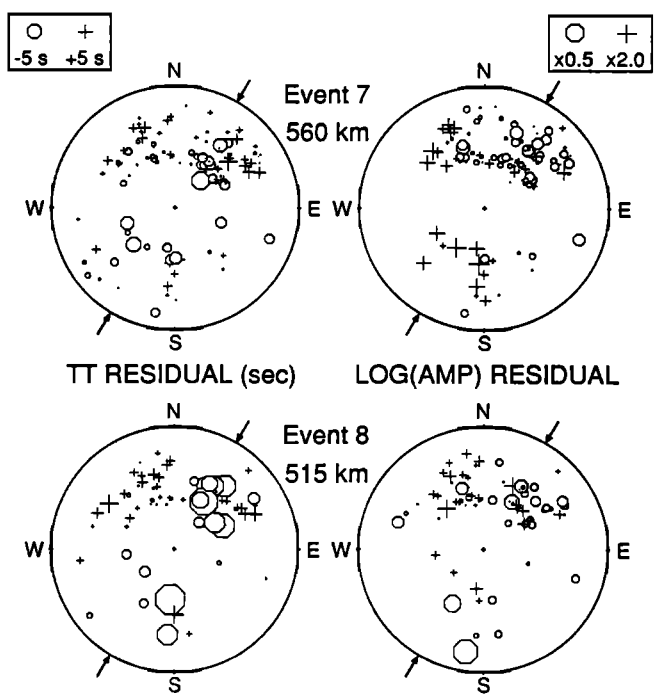

Fig. 4. Travel time and logarithmic amplitude residual spheres for events 7 (top) and 8 (bottom). Travel time residual spheres are on the left, and amplitudes are on the right. Data include *S* and *ScS* observations, with *S* plotting closest to the circumference and *ScS* plotting closer to the center. Symbols are as in Figure 3, with the symbol sizes linearly scaled relative to the key. Note that both the travel time and log (amplitude) residuals are demeaned prior to plotting and that the number of travel time observations is generally greater than the number of amplitude residuals, due to the bounds on the radiation pattern correction described in the text. Arrows on the perimeter of each sphere delineate the approximate strike of the Kurile slab.

The right side of Figure 4 shows the log(amplitude) residual spheres for events 7 and 8. Note that several stations for which travel times are measured are not included in the amplitude sphere. This is because proximity to the nodal planes make their corrected amplitudes unreliable. These are the first long-period *S* wave amplitude residual spheres of which we are aware, and potentially these can be used to place new constraints on slab structure. A major obstacle to quantitatively analyzing amplitude variations for complex three-dimensional structures is the difficulty of calculating reliable synthetic seismograms for such structures. Accurate numerical procedures (e.g., the finite difference method used here) can be used for two-dimensional structures, but three-dimensional techniques are still under development [*Cormier*, 1989; *Witte*, 1989]. *Cormier and Kim* [1990] have used simple geometric optics to compute travel time and amplitude patterns for several three-dimensional slab models, which can be used as a qualitative guide for slab effects. The geometric amplitude calculations are dominated by slowly varying patterns with minimum amplitudes at azimuths obliquely down the dip of the slab structure. This feature correlates well with early arrival times in the synthetic travel time patterns [*Cormier and Kim*, 1990] and is therefore consistent with defocusing by the high-velocity slab structure. At shorter spatial scales, the amplitude patterns show rapid variations, with regions of focusing near the strike of the slab, caused by caustics and multipathing along the gradients at the top and bottom of the structure. *Silver and Chan* [1986] suggested that such effects cause the waveform anomalies that they observe along the strike of the Kurile slab. These small-scale patterns are not well correlated with the travel time anomalies [*Cormier and Kim*, 1990]. The complexity of the amplitude patterns makes it extremely difficult to assess the amplitude residual spheres for coherent structure. In addition, *Cormier and Kim* [1990] show that while slowly varying patterns are robust, the rapid amplitude fluctuations near caustics are highly sensitive not only to the velocity gradients in the slab but also to the precise lateral location of the source within the slab.

This increase in the number of model parameters makes it difficult to model observations from an imperfectly known location.

We can make the qualitative assessment that the observed amplitude patterns (Figure 4) are not dominated by the degree 2 azimuthal trend that is present in the travel times and that there is greater variability between events. There does appear to be a region of consistently low-amplitude arrivals in the north, weakly correlated with the early arrivals in this direction. This may be consistent with defocusing, but the pattern is not mirrored in the south as it is in the travel times. These two events are located at the northeastern end of the Kurile slab, so any slab signature to the south should be as strong or stronger than the pattern to the north, as has been suggested on the basis of travel times [*Jordan*, 1977; *Creager and Jordan*, 1984]. There is a suggestion of a ray parameter trend apparent in the northwest quadrant of the spheres that we will analyze in depth in the next section. In general, however, the scatter in the data makes it difficult to assess the long-wavelength characteristics of the amplitude spheres.

Complete discussion of the full residual spheres for many other events will be presented in a future paper. We will concentrate here on a limited portion of the residual spheres that presently can be quantitatively modeled with reliable techniques.

DOWNDIP ANALYSIS

Jordan [1977] observed that the *S* wave travel time residual sphere for event 8 has a strong ray parameter (takeoff angle) trend in the northwest quadrant (see Figure 1, this paper, and Figures 6 and 8 of *Jordan* [1977]), with the *ScS* arrivals being fast relative to the *S* arrivals at azimuths in the downdip direction. This is manifested as a *ScS-S* differential travel time anomaly at the stations to the northwest, so it is clearly not due to receiver structure. This trend, which is apparent in our residual spheres as well (Figure 4), was interpreted by Jordan to be due to the *ScS* ray paths preferentially sampling a near-vertical slab extension in the lower mantle beneath the event. A large portion of the European and Middle Eastern WWSSN stations providing these observations falls within 45° of the downdip direction of the Kurile and Japan slabs, an azimuth range in which most proposed deep slab models (e.g., Figure 1*b*) predict simple, observable trends in both amplitude and travel time. The three-dimensional calculations of *Cormier* [1989] and *Cormier and Kim* [1990] predict smooth amplitude and travel time variation with distance (ray parameter) throughout these azimuths, and the two-dimensional calculations of *Vidale* [1987] (Figure 1c) and *Weber* [1990], which are appropriate for this downdip geometry, predict very similar patterns. This is, of course, partly the result of the very smooth slab structures that have been investigated, and more complex structures may produce less regular amplitude patterns. Unlike the along-strike azimuthal patterns, the amplitudes in this portion of the residual sphere appear to be fairly stable for variations in the lateral source location within the subducting slab (for long-period energy), allowing us to investigate structural aspects of the slab, such as strength of the anomaly, the velocity gradients present, and the depth of slab penetration.

Constraining our present study to the near slab-dip azimuth range simplifies our data processing, as bias in the travel time residuals due to epicentral location error should be relatively constant over the data subset and thus may be ignored. Large depth errors are required to cause significant trends with takeoff angle. For example, a 20-km depth error gives rise to only an average *ScS-S* anomaly of less than 0.5 s at these distances, and as discussed above, we believe that the potential errors in the depths

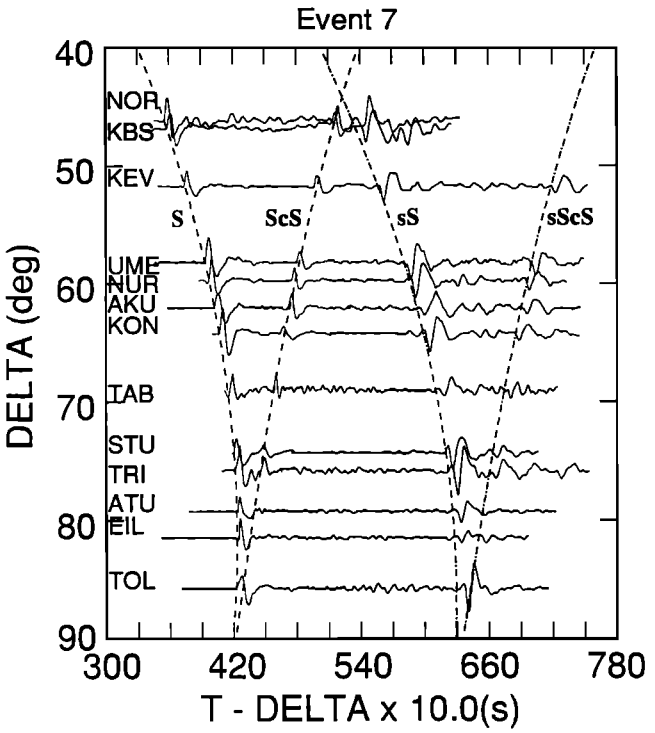

Fig. 5. Example profile of seismograms from European WWSSN stations for event 7. Travel time curves calculated for the PREM 1-s structure are displayed for *S*, *ScS*, *sS*, and *sScS*, and the seismograms are arranged so that each *S* arrival lines up with the *S* travel time curve.

of our sources is typically much less than 20 km. Source relocation of the magnitude reported by *Creager and Jordan* [1986] have almost no effect on the differential travel times *ScS-S* and *sScS-sS* in the range of interest. This is because relocation can remove only slowly varying trends from the residual sphere. Vertical variations do result in large baseline shifts in travel times between downgoing (*S*, *ScS*) paths and upgoing (*sS*, *sScS*) paths, but errors in upper mantle velocity structure may as well; therefore, we do not attempt to analyze absolute differences in travel time between these two groups.

A representative event profile of *SH* seismograms recorded in the near slab dip direction (European and Middle Eastern WWSSN stations) is presented in Figure 5. The traces are aligned such that the *S* first break coincides with the arrival time predicted for Preliminary Reference Earth Model (PREM). Even at this scale, the relatively early arrival of *ScS* phases is striking. The relatively accurate alignment of *sS* indicates that this is not due to a substantial error in source depth; improving the timing of the *sS* branch requires a slightly deeper source but would reduce the *ScS-S* anomalies by less than 0.2 s. Note that the *sS* and *sScS* observations for this event are very clear, allowing travel time and amplitude measurements to be made with good precision.

The advantage of including both upgoing and downgoing phases for this analysis is shown schematically in Figure 6. Ray paths for the *S*, *ScS*, *sS*, and *sScS* phases from a 515 km deep source are traced through the PREM structure to distances of 55° to 85°. The approximate geometry of the Kurile slab proposed by *Creager and Jordan* [1984] (Figure 1b) is superimposed. Figure 6 clarifies *Jordan's* [1977] interpretation of the strong travel time gradient from *S* to *ScS* observed for the Kurile events in Figure 4. The *ScS* rays have longer paths than the *S* rays within the proposed slab extension and therefore would be faster, as observed. This does require that the slab steepen in dip.

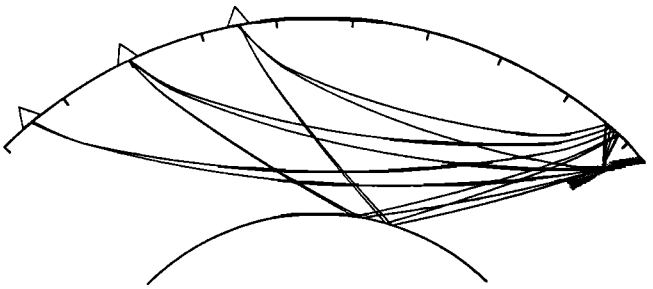

Fig. 6. Ray path diagram depicting preferential sampling of various mantle regions by the phases employed in this study. Rays are traced from a 515-km-deep source to receivers (triangles) at epicentral distances of 55°, 70°, and 85°. Beyond 79°, we cannot measure core reflected phases on the long-period records. Hatched region schematically outlines a slab structure with the approximate geometry proposed for the Kurile slab by *Creager and Jordan* [1984].

Alternatively, note that the *S* wave ray paths in this distance range have turning points several hundred kilometers above the core-mantle boundary, allowing for the possibility that the ray parameter dependence of the travel times is produced by large-scale heterogeneity in the lower mantle sampled by *ScS* but not *S*, or vice versa.

Figure 6 also demonstrates that the *sS* and *sScS* rays leave the slab at an upward angle, exiting the slab quickly and never sampling the proposed deep slab extension, so the travel times and amplitudes of these phases should be free of slab induced anomalies. In addition, note that once *sScS* and *ScS* are far from the near-source region, they have very similar paths in the deep mantle and near the receiver. The same is true for the *sS* and *S* paths. These simple relationships lead to the hypothesis that any relative patterns in the *sS* and *sScS* travel times and amplitudes may be used to correct the *S* and *ScS* patterns for deep and receiver mantle structure, thereby isolating any near-source signature in the *S* and *ScS* patterns. This applies only for the azimuth range near the down slab-dip direction, since the upgoing phases may encounter the slab at other azimuths. An obvious potential problem is the possibility of misinterpreting heterogeneous or anisotropic [*Ribe*, 1989] structure in the mantle wedge above the slab sampled by the *sS* and *sScS* phases as deep mantle structure and erroneously correcting for it. Because of this possibility, we analyze the data both with and without applying empirical deep mantle corrections based on the upgoing phases. However, as discussed below, the observations indicate that the gradational effect of the mantle wedge on the *sS* and *sScS* differential travel time and amplitude patterns is minimal, as might be expected given the tightly bundled *sS* and *sScS* ray paths in the region (Figure 6).

One of our primary methods of data presentation and model comparison will be on a "rose"-type diagram (Figure 7) that is essentially a two-dimensional cross section through a residual sphere. The plane of the cross section is along the down slab-dip direction: 301° for the Kurile slab [*Fischer et al.*, 1988] and 275° for the Japan slab [*Creager and Jordan*, 1984; *Fischer et al.*, 1988]. Observations with azimuths within ±45° of the downdip direction are included in the projection. Residuals are plotted at an angle corresponding to their takeoff angle and a radius corresponding to the relative size of the anomaly. Takeoff angle varies from 0° vertically down to 180° vertically up. On the travel time diagrams, the outer and inner circumferences correspond to a travel time residuals of +5 s and -5 s, respectively, and the circle between them represents the mean of the observations, i.e., a travel time residual of 0 s. On the amplitude diagrams, the residuals range from x2 at the outer circumference to x0.5 at the inner circumference, with a mean of x1 marked by the intermediate semicircle. The *S* and *ScS* observations are demeaned as a group so that variations within the group can be examined. The anomalies are plotted at takeoff angles that are corrected to preserve the angle between the ray and the plane of the proposed slab model. This procedure is just a mapping onto a two-dimensional geometry that minimizes distortion in the observed travel time and amplitude patterns that would result from inclusion of observations recorded at azimuths away from the purely downdip geometry. This projection should maximize any slab signature but may slightly distort any deep mantle trends. Of course, actual takeoff angles in a heterogeneous Earth may differ from these reference model calculations, but this model dependence is part of the problem. The *sS* and *sScS* observations are also demeaned as a group to emphasize their relative

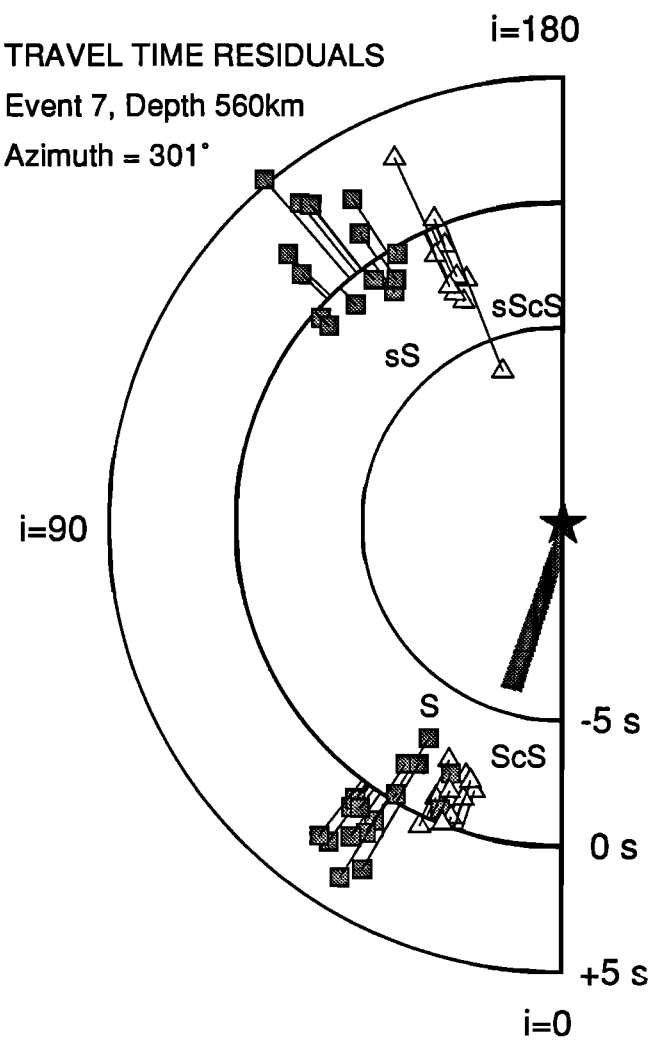

Fig. 7. Travel time observations in the azimuth range 45° on either side of the Kurile slab-dip direction, plotted on a residual rose diagram. Diagram represents a cross section through the residual sphere in Figure 4, at an azimuth of 301°. Takeoff angle (*i*) ranges from 0° to 180°, thereby including *sS* and *sScS* observations in addition to *S* and *ScS*. The takeoff angles for *S* and *ScS* (calculated for PREM) have been corrected to account for the projection into the plane of the cross section. The downgoing and upgoing data are demeaned separately, with relative variations ranging from 5 s slow (outer circumference) to 5 s fast (inner circumference). *S* and *sS* residuals are plotted as squares, and *ScS* and *sScS* residuals are plotted as triangles. Hatched region approximates the lower mantle slab dip preferred by *Fischer et al.* [1988], and tie lines connect each data point to the mean circle at the corrected takeoff angle.

variations, and are plotted at their true takeoff angles (calculated using PREM). All observations are connected to the mean circumference by a tie line that defines the corrected takeoff angle of the observation. The hatched region projecting radially from the source schematically represents the dip of potential deep slab structures extending below the source: for 515-570 km deep events, this geometry is as proposed for the corresponding slab model from *Fischer et al.* [1988]; for 380-400 km deep sources, the geometry is that of the Wadati-Benioff zone between the source and 600 km depth.

The travel time residuals plotted in Figure 7 clearly show the *S* to *ScS* gradient, with steeper (*ScS*) rays being faster, that was apparent in the northwest quadrant of the residual sphere in Figure 4. This trend appears to be geometrically consistent with a deep slab structure similar to that proposed by *Creager and Jordan* [1984] and *Fischer et al.* [1988]. However, note the similar trend in the surface reflected phases, with *sScS* being fast relative to *sS*. The data in Figure 5 indicate the correspondence of relatively early *ScS* and *sScS* phases at a common station. The simplest interpretation for the similarity between the two trends is that some portion of it is due to the common paths shared by *S* and *sS* and by *ScS* and *sScS* in the deep and near-receiver mantle (see Figure 6).

Slab Models

With these preliminary observations in mind, we now consider a suite of slab models (Figure 8) for which we calculate synthetic seismograms in the two-dimensional downdip geometry. These models provide travel time and amplitude calculations which we can compare with our observations. Figures 8*a*-8*c* represent variations of the Kurile slab models proposed by *Creager and Jordan* [1984, 1986] and *Fischer et al.* [1988]. These slabs have the general properties of a 52° dip above 500 km, steepening to 72° below 500 km. Figure 8*a* represents the *S* wave version of the simple, undeformed Kurile slab preferred by *Creager and Jordan* [1986] and refined by *Fischer et al.* [1988], which remains the most widely discussed model for deep slab structure. For this reason, all of our observations will initially be compared with predictions from this model. For brevity, this slab model will be designated as the "long, thin" slab.

Figure 8*b* represents a slab that thickens by a factor of 3 over a range of 150 km as it passes through the 670-km discontinuity. *Fischer et al.* [1988] found that modeling *P* wave travel time residual spheres alone could not resolve variations in slab thickness of this type, and this model therefore fits the *P* wave travel time observations nearly as well as the model in Figure 8*a*. We term these models the "fat" slab models. *Gurnis and Hager* [1988] showed that an increase in viscosity at the 670-km discontinuity could produce slab deformation and thickening in excess of a factor of 3, so it is important to determine if the travel time and amplitude observations prefer this type of model over a thin, undeformed slab. As pointed out by *Vidale* [1987] and *Cormier and Kim* [1990], the reduced lateral velocity gradients present in the thickened slab defocus the wave front less

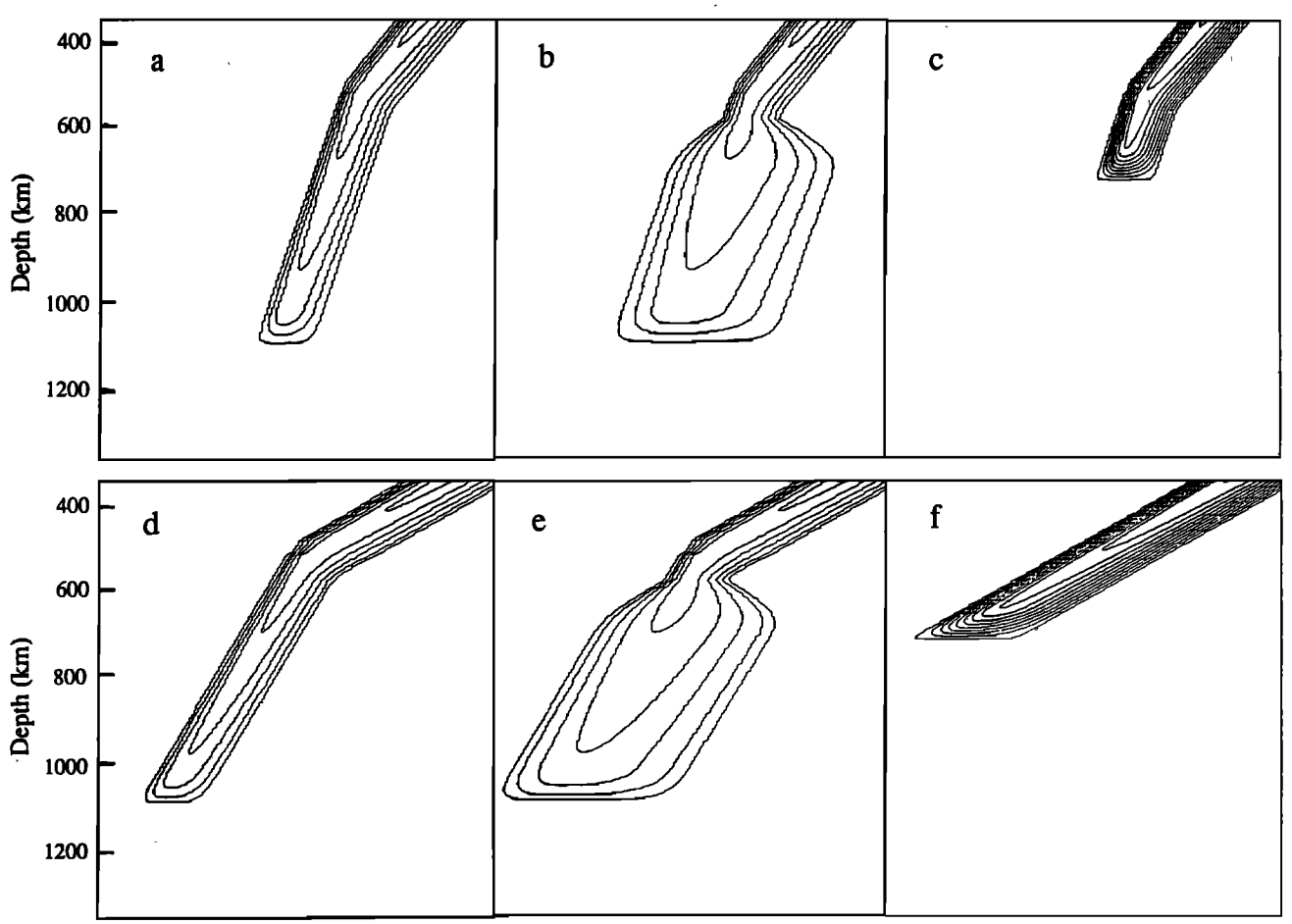

Fig. 8. Slab velocity structures (expressed as perturbations to PREM) for which synthetic travel time and amplitude residuals are computed by a finite difference method. These models are based on the models proposed by *Creager and Jordan* [1984, 1986] and *Fischer et al.* [1988]. (*a*) Long, thin, (*b*) fat, and (*c*) short Kurile slab models. (*d*) Long, thin, (*e*) fat, and (*f*) short Japan slab models. Contours represent percentage variation, ranging from 0% to 10% at 2% intervals for the long, thin and fat models and from 0% to 20% at 2% intervals for the short models.

efficiently than the thinner slab models, while the integrated travel time anomaly remains approximately the same, and therefore amplitude observations may be more diagnostic of slab thickness than travel times for simple slab geometries.

The third type of model that we explore is shown in Figure 8*c*. Given the possibility that we may be able to explain much of the travel time patterns with deep and near-receiver mantle structure, we explore models which terminate near the 670-km discontinuity, referred to as the "short" slab models. Presumably the slab would deflect horizontally near 670 km depth if it cannot penetrate into the lower mantle, but our ray paths cannot resolve such structure. Even if we cannot explain the travel time anomalies by deep mantle or receiver effects, the short slab model may be relevant. *Anderson* [1987*a*] has argued that anisotropy or isobaric phase changes within the cold slab structure may substantially increase the slab's velocity anomaly beyond that produced by the thermal anomaly alone, and therefore a short, very fast slab may be appropriate. In our short models, the strength of the anomaly is set at twice that of the deep penetrating slabs, so that the azimuthal travel time observations of *Creager and Jordan* [1984] and *Fischer et al.* [1988] are approximately preserved. Note that the short slab model for the Kuriles retains the increase in dip between 500 and 550 km, as this feature is consistent not only with the modeling of *Creager and Jordan* [1986] but also with the trend of Wadati-Benioff zone earthquakes in the central Kurile arc [*Veith*, 1974].

Figures 8*d*-8*f* depict the same categories of slab models adjusted to match the geometry of the Japan slab proposed by *Creager and Jordan* [1984, 1986]. These models have a dip of 30° above 550 km and a dip of 60° below 550 km. Note that the "short" Japan slab model does not incorporate this change in dip, as the hypocenters of 550-600 km depth events beneath the Sea of Japan do not indicate such a change.

A fundamental ambiguity in modeling deep slab structure is in estimating the strength of the velocity anomaly. *Creager and Jordan* [1986] modeled the travel time residuals from intermediate depth events to empirically determine the appropriate value of dV_P/dT to map their thermal models into velocity structures. For the Kurile slab, the resulting models have slab velocities ranging from approximately 5.7% faster than surrounding mantle at 350 km depth to 2.8% fast at 1150 km depth. For the Japan slab, the range is from 5.1% fast at 350 km depth to 3.2% fast at 1000 km depth. *Anderson* [1987*a*] has argued that these values are low due to unmodeled isobaric phase changes, and cites a variety of slab anomaly estimates that vary substantially with depth, but in general indicate a V_P anomaly of approximately 5% at intermediate depth [e.g., *Engdahl and Gubbins*, 1987] increasing to approximately 10% for the 600-700 km depth range [*Fitch*, 1975]. In addition, even assuming that the strength of the *P* wave anomaly is well determined, *Vidale* [1987] argues that the appropriate lower mantle anomaly for S waves is approximately twice as strong as that for *P* waves, based on comparisons of lateral velocity variations in the lower mantle [*Anderson*, 1987*b*] that indicate $\partial \ln V_s / \partial \ln V_p > 2$; recent thermodynamic calculations [*Agnon and Bukowinski*, 1990] support this conclusion.

The modeling presented here adopts an intermediate position within these estimates. Our deep models have a peak velocity anomaly of 10% at 350 km depth, which decreases linearly to approximately 5% at 1100 km depth. Note that these values represent the largest anomaly within the slab; the slab models are constructed with an asymmetric sine cross section, thus the average anomaly at each depth within the slab will be $2/\pi$ (0.64) times these values. The strength of the anomalies are similar to shear wave models studied by *Jordan* [1977], *Vidale* [1987], and *Cormier and Kim* [1990].

To generate amplitude and travel time calculations for these models, we impose the velocity anomaly models in Figure 8 onto an Earth-flattened PREM structure and calculate long-period synthetic seismograms at a suite of takeoff angles. The frequency content of the synthetics is comparable to that of the observations. Travel time and amplitude residuals are then measured relative to synthetics calculated for the PREM structure. These residuals are demeaned; that is, they include only relative variations, so they can be directly compared to the downdip data residuals. Travel time baselines are, in general, on the order of 6 s fast relative to PREM, and the amplitude baselines are on average approximately 0.6 times the PREM amplitude.

Synthetics are calculated for two source depths for each slab model: 380 km and 515 km in the Kurile slab models and 400 km and 560 km in the Japan slab models. Sources are located in the fastest (coldest) portion of the slab. To test the dependence of our results on this choice of source location, we have calculated seismograms for source locations laterally removed up to 20 km from the center of the slab in each direction. We find that over the range of takeoff angles presented here, the amplitude (or travel time) versus takeoff angle behavior is essentially constant with the variation in source location. Baseline shifts occur for the entire range of takeoff angle, but no differential behavior is observed. This is a major benefit of using long-period data for this study, as *Weber* [1990] has demonstrated that short-period amplitude calculations for simple slab models are highly dependent on the precise location of the source within the slab, thereby adding a poorly constrained model parameter to analyses using short-period data.

As mentioned above, the short models analyzed here have a peak velocity anomaly of 20%. Due to the rapid termination of these slab models beneath the deep focus sources, even this extreme anomaly produces very limited amplitude and travel time variation with takeoff angle, and numerical tests indicate that the differential patterns are similar for weaker slabs. Therefore, the choice of such a strong velocity anomaly will not significantly bias our results for these models.

Finally, we note that event 7, which has an ISC focal depth of 560 km, is compared to synthetics calculated for a source depth of 515 km. Synthetics calculated for a source depth of 560 km show essentially no differences in relative amplitude or travel time variation with takeoff angle relative to the 515-km synthetics, so for simplicity the latter calculations are used. Likewise, observations for event 14 (source depth of 402 km) are compared to synthetics calculated for a 380 km source depth.

Travel Time and Amplitude Observations

Figures 9*a-d* show travel time and amplitude residual rose diagrams for the four deep events that have the most complete upgoing and downgoing ray coverage from the Kurile slab. These diagrams are similar to the example in Figure 7, except that synthetic travel time and amplitude anomalies calculated for the long, thin slab are plotted along with the downgoing data. For each event, travel time residuals are plotted on the left, and amplitude residuals are on the right.

Several observations are apparent in these figures. First, note that the travel time residuals from all four events show a strong takeoff angle dependence, with the more steeply diving *ScS* observations being fast relative to *S*. The strength of this trend does not vary much with depth of the event; the trends for the events at 515 and 560 km depth (Figures 9*a* and 9*b*) are about the

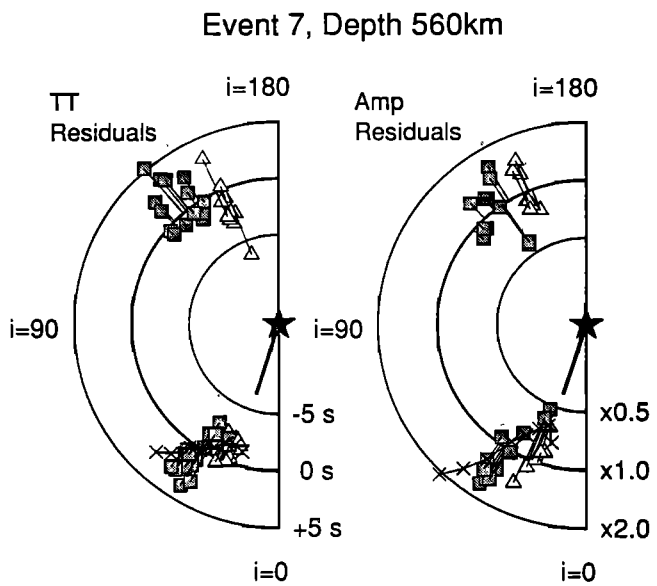

Fig. 9*a*. Travel time and amplitude residual rose diagrams for event 7, using the same plotting conventions outlined in Figure 7. The travel time diagram is on the left, the amplitude diagram is on the right. The synthetic travel time and amplitude residuals calculated for the long, thin slab model are now included as crosses with the *S* and *ScS* data.

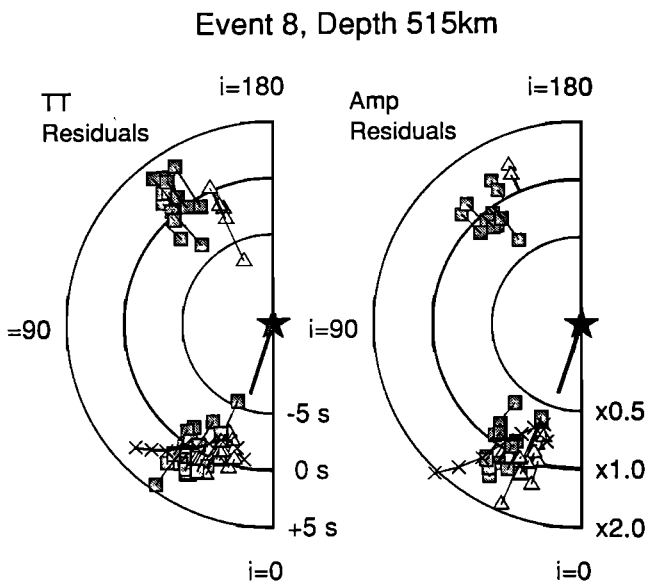

Fig. 9*b*. Same as Figure 9*a*, but for event 8.

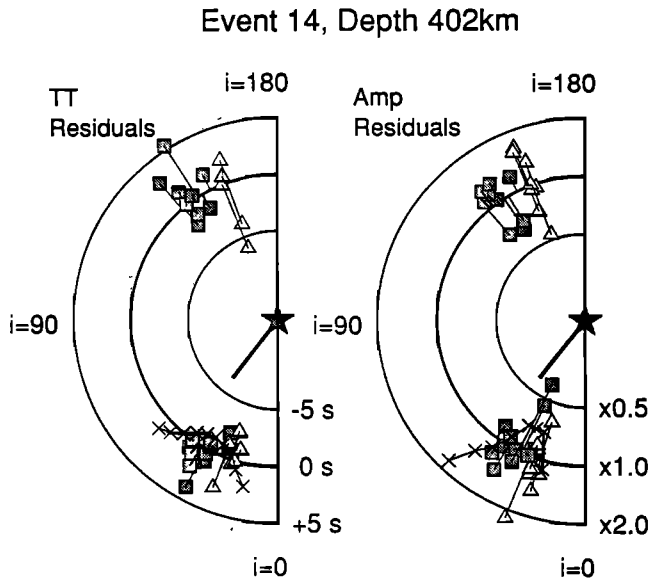

Fig. 9*c*. Same as Figure 9*a*, but for event 14.

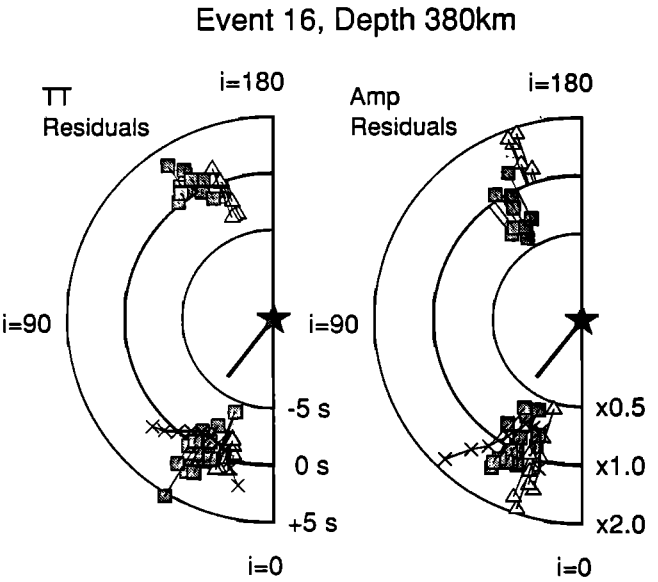

Fig. 9*d*. Same as Figure 9*a*, but for event 16.

same as those for the 380- and 402-km-deep events (Figures 9*c* and 9*d*). This is significant in evaluating these trends for slab structure, as the travel time residuals calculated for the long, thin slab model predict a weakening of the *S* to *ScS* trend as source depth decreases due to the change in slab dip (contrast the crosses in Figure 9*a* against those in Figure 9*c*, for example). This lack of depth dependence of the observed travel time residuals is consistent with observations made along strike of the Kurile slab by *Lay* [1983] and *Schwartz et al.* [1991] and is at odds not only with the calculations presented here, but also with the *P* wave residual sphere observations of *Creager and Jordan* [1984] for events in this region.

The travel time residuals for the upgoing phases *sS* and *sScS* also show consistent behavior for all four events, with the takeoff angle trend in residuals from *sS* to *sScS* mirroring the trend in the *S* and *ScS* residuals. However, the correlation between *S* and *sS* residuals and between *ScS* and *sScS* residuals is poor for these events (R=0.23), indicating that the scatter in the data is fairly high. As we see below, if the varying path behavior is further accounted for, much of the scatter is removed, and more coherent relative behavior becomes apparent.

The amplitude residuals in Figure 9 show greater scatter and less coherent structure than the travel times. The *S* and *ScS* amplitudes for event 7 (Figure 9*a*) show a strong trend similar to that observed in the travel times that is fairly consistent with the defocusing of *ScS* predicted for the long, thin slab model. Event 8 (Figure 9*b*) also shows a slight defocusing of *ScS* relative to *S*, but the trend is weaker than that calculated for the deep slab. Events 14 and 16 (Figures 9*c* and 9*d*) have more scatter and are difficult to evaluate, but the observations appear to lack any strong trend. This does not appear compatible with the predictions of the long, thin slab model.

The upgoing amplitude patterns are even more difficult to assess than the downgoing amplitudes. Events 7, 8, and 14 are all similar in that *sS* and *sScS* lack a well-developed trend. Event 16 shows a strong trend, with *sS* observations substantially smaller than *sScS* observations, which does not have a counterpart in the downgoing phases. Potential explanations for this trend include a strongly focusing/defocusing effect or heterogeneous anelastic structure in the mantle wedge. Alternatively, the isolated occurrence of this trend among a group of events that show fairly good coherence in other travel time and amplitude patterns perhaps indicates a source anomaly rather than a structural effect. Due to uncertainties in the amplitude baselines between the upgoing and downgoing observations, the *sS* and *sScS* amplitudes were not included in the focal mechanism determinations. Thus, this isolated trend may be indicative of an incorrect radiation pattern correction that preferentially affects the upgoing phases.

The travel time and amplitude residual rose diagrams for the three best recorded Japan slab events are shown in Figure 10. These diagrams only show the anomalies for downgoing paths because of poor *sS* and *sScS* radiation for all of these events. Due to the change in strike of the Japan slab relative to the Kurile slab, many of the European stations are no longer in the downdip direction, and thus even the *S* and *ScS* data are relatively sparse. Despite this sparsity, the observations still cover a range of takeoff angles that should be diagnostic of slab structure (note the calculated trends projected on the diagrams), so we include them for completeness. Event 6 is an event at approximately 400 km depth, in a portion of the slab with a very shallow (approximately 30°) dip. Thus, as indicated by the calculations for the long, thin slab model, this event should have very distinct travel time and amplitude patterns relative to the other (deeper) events. The travel times do not seem to support this prediction, although the scatter and sparse data distribution make it difficult to assess the observations. The amplitudes for event 6 do show a strong trend, with the *S* observations at the largest takeoff angles being substantially smaller than the other observations, as predicted by the long, thin slab model. The amplitudes for events 13 and 18 are quite sparse and scattered, but they clearly show a change in pattern from the shallower event that is in qualitative agreement with the long, thin slab model.

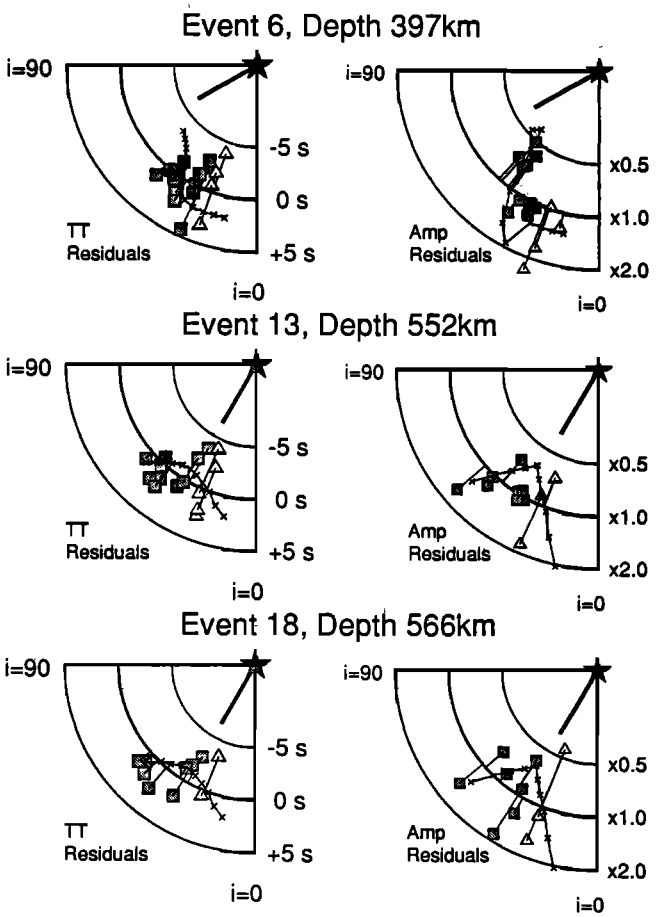

Fig. 10. Travel time and amplitude residual rose diagrams for three deep Japan events. *sS* and *sScS* data for these events is very poor, so the diagrams only include a downgoing takeoff angle range of 0° to 90°. Again, the crosses indicate the predicted patterns for the long, thin slab model.

While the diagrams in Figures 9 and 10 indicate that some significant trends exist in the downdip travel time and amplitude observations, it is clear that the scatter in the data limits our ability to constrain the slab models. However, for our two-dimensional geometry, much of the observed and predicted variation in the travel time and amplitude residuals involves relative behavior between *S* and *ScS* (or *sS* and *sScS*), and we thus can make a final correction to the data.

As depicted in Figure 6, the *S* and *ScS* observations at a given station have similar paths in the receiver mantle and crust, which may result in a common shift in the travel time or amplitude residuals of the two phases. The same is true for the *sS* and *sScS* observations. This common shift can be corrected for by removing the mean of the two upgoing or downgoing observations at each station. This preserves any takeoff angle trends in the data while reducing the variation due to heterogeneity that effects both *S* and *ScS*, or *sS* and *sScS*, recorded at a given station. This procedure is essentially a variant on differential time analysis, which has been used in many studies to isolate lower mantle structure [e.g., *Jordan and Lynn*, 1974; *Lay*, 1983]. In addition, we can stack observations from sources with similar depths.

Figure 11 shows the travel time residuals for the four deep Kurile events. In Figure 11*a*, the demeaned pairs of *sS* and *sScS* observations are plotted against ray parameter. Parameterization by ray parameter inherently accounts for variation in focal depth of the four events, allowing us to stack all of the *sS* and *sScS* observations to obtain a single trend. It is clear from the common slopes of the *sS* to *sScS* tie lines that much of the scatter apparent in the upgoing travel time residuals in Figure 9 is due to common path variations, and the data now display a very strong trend. The coherence of the trend over the four events is striking, and it is clear that all of the *sScS* travel times in the downdip direction are fast relative to the *sS* travel times to the same station. Similarly, the *ScS* to *S* behavior displays a clear trend (Figure 11*b*), and it appears quite similar to the *sScS* to *sS* trend. The linear correlation coefficient between the station demeaned *sS* and *S* observations, and *sScS* and *ScS*, has improved from 0.23 prior to demeaning to 0.80 after demeaning. The simplest interpretation of this trend is that it is a result of a laterally extensive region of high velocity near the core-mantle boundary or a region of anomalously slow velocity in the middle-lower mantle. In fact, *Tanimoto* [1990] found that the long wavelength velocity structure just above the core-mantle boundary beneath Eurasia is fast relative to PREM, and a laterally discontinuous high-velocity layer in *D*" has been proposed for this region [*Lay and Helmberger*, 1983b; *Baumgardt*, 1989; *Weber and Davis*, 1990].

Despite the strong correlation between the upgoing and downgoing phases, we explore the possibility that mantle wedge or crustal structure near the surface reflection points of the

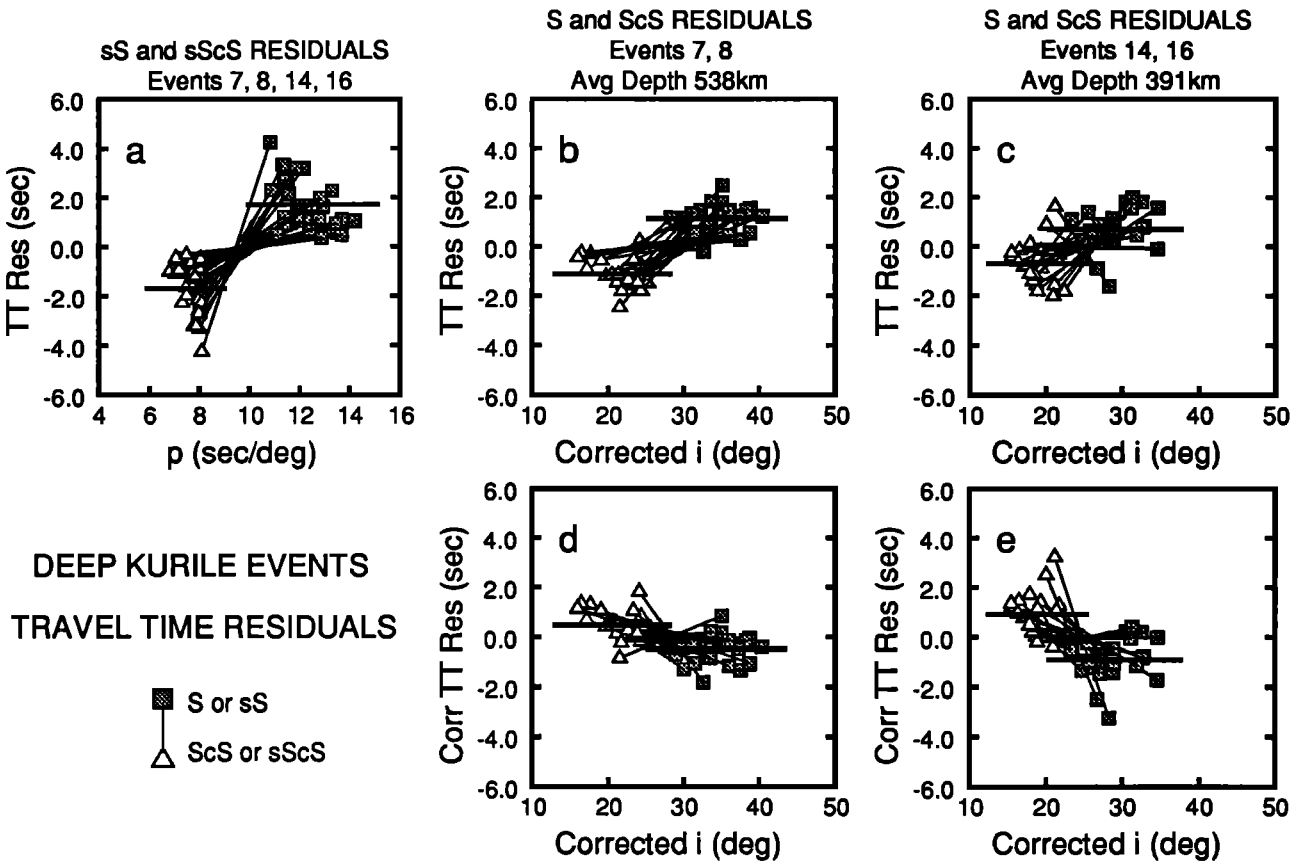

Fig. 11. Downdip travel time observations from deep Kurile events corrected for station behavior observed in each *S* and *ScS* (or *sS* and *sScS*) pair. Tie lines connect each *S* and *ScS* (or *sS* and *sScS*) pair. Solid horizontal lines delineate the mean of each of the *S* (*sS*) and *ScS* (*sScS*) populations. (*a*) Stack of pair-demeaned *sS* and *sScS* travel time residuals versus ray parameter for events 7, 8, 14, and 16. (*b*) Stack of *S* and *ScS* travel time residuals versus takeoff angle (corrected for projection into downdip azimuth) for events 7 and 8. (*c*) Same as Figure 11*b*, but for events 14 and 16. (*d*) Data from Figure 11*b* corrected for the deep mantle trend observed in Figure 11*a*. (*e*) Data from Figure 11*c* corrected for the trend observed in Figure 11*a*.

upgoing observations could be responsible for the *sS* to *sScS* trend. Figure 12 is a map of the Sea of Okhotsk with the *sS* and *sScS* travel time residuals for the four Kurile events plotted at their surface bounce points. It is clear that the observations do not span an ocean-to-continent transition or any other major structural feature. In addition, the close proximity of the *sS* and *sScS* bounce points (often within 200 km distance) and the spatial distribution of the four events would require extremely strong gradients or anisotropy with a complex, contorted geometry in the upper mantle to explain the rapid variation from *sS* to *sScS*. When this required complexity is contrasted with the simplicity of a laterally extensive anomalous velocity region in the lower mantle, and when the high correlation between the upgoing and downgoing travel time residuals is considered, it is apparent that the deep mantle is the most reasonable interpretation of the travel time anomaly. We will therefore apply the *sS* and *sScS* observations as an empirical correction for the deep mantle structure.

The demeaned *S* and *ScS* travel time residuals for events 7 and 8 are stacked in Figure 11*b* versus takeoff angle corrected for azimuth variation. The observations for the shallower events 14 and 16 are plotted in Figure 11*c*. Again, the station demeaning procedure has substantially reduced the scatter in the observations, and the *ScS* to *S* shift is well defined. Interestingly, the *ScS* to *S* gradient for events 14 and 16 is slightly reduced relative to the trend for events 7 and 8. This depth dependence was not apparent in the data prior to the station pair-demeaning procedure. Although the change in trend is small, such a depth dependence in

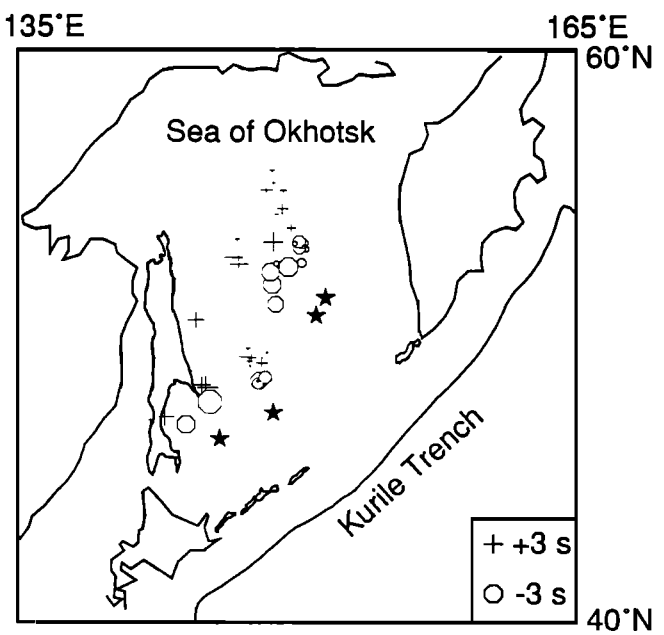

Fig. 12. Mercator projection of the Sea of Okhotsk region, with the *sS* and *sScS* travel time residuals observed in Figure 9 projected to the surface bounce point corresponding to each observation. Crosses and circles represent slow and fast, respectively, linearly scaled to the size of the residuals, and the stars indicate the epicenters of the events. Residuals from each event have been demeaned to highlight relative variations.

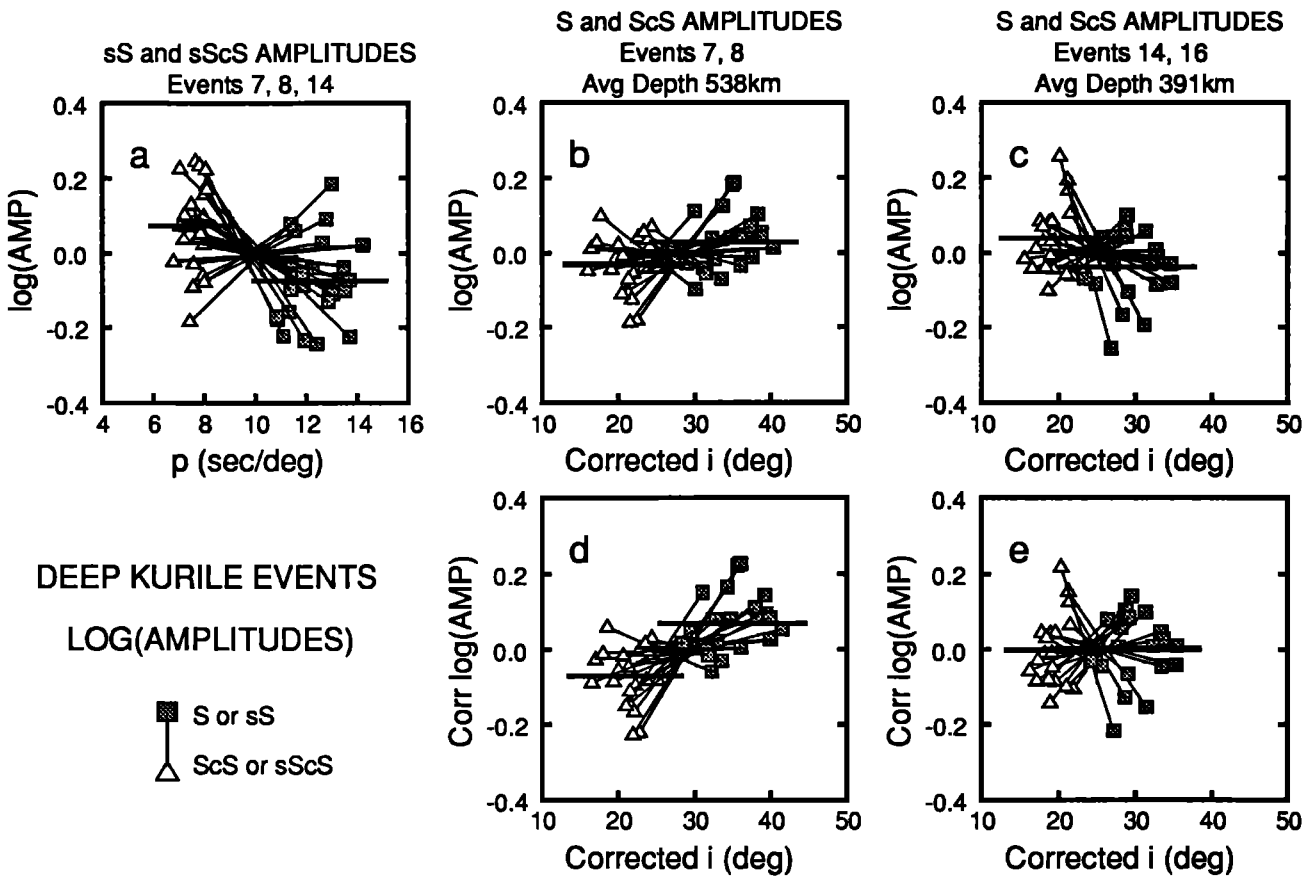

Fig. 13. Same as Figure 11, except for amplitude residuals instead of travel time residuals. (*a*) *sS* and *sScS* amplitudes versus ray parameter for events 7, 8, and 14. (*b*) *S* and *ScS* amplitudes versus corrected takeoff angle for events 7 and 8. (*c*) *S* and *ScS* amplitudes for events 14 and 16. (*d*) Data from Figure 13*b* corrected for deep mantle trend in Figure 13*a*. (*e*) Data from Figure 13*c* corrected for trend in Figure 13*a*.

the travel time patterns is predicted for the steepening long, thin slab models, as discussed earlier.

Figures 11*d* and 11*e* show the *S* and *ScS* travel time observations for the same event groupings, now corrected for deep mantle structure using the *sS* and *sScS* observations. Since the *sS* and *sScS* observations separate with significantly different means (1.6±0.4 s and -1.6±0.4 s, respectively, at a 99% confidence level) but considered separately, neither *sS* nor *sScS* show a ray parameter trend, we simply use the mean of the *sS* residuals as corrections for the *S* observations, and likewise correct *ScS* residuals with the *sScS* mean. For events 7 and 8 (Figure 11*d*), the resulting trend in travel time residuals with takeoff angle has a reversed polarity, with the *S* observations now fast relative to the *ScS* observations, although the strength of the trend is substantially reduced, with a mean offset of less than 1 s total. Events 14 and 16 also show a reversed trend (Figure 11*e*), somewhat stronger than that observed for the deeper events (mean offset of 1.4 s total). These results have profound implications for the proposed models of deep slab structure. The fact that the *sS* to *sScS* travel time residual variation is larger than that observed for the *S* and *ScS* paths indicates that the deep mantle structure thoroughly masks the travel time signature of the slab structure and was entirely responsible for the *S* to *ScS* gradient that can otherwise be explained by slab models that steepen in dip at 500 km depth. Once this deep mantle signature is removed, the resulting travel time residuals of the 380 to 402-km-deep events have patterns that would be expected for a slab with the known dip of the Wadati-Benioff zone in this region. Farther down the slab by approximately 150 km, the deeper events show a similar trend with takeoff angle, and the magnitude of the trend is reduced by 33%. This is clearly incompatible with the strong trend predicted in Figure 9*a* for the long, thin slab model, which calls for much more negative *ScS* residuals (relatively) than *S* residuals. We will compare the resultant trends to the other slab models after we have presented the amplitude observations.

Figure 13 presents the station demeaned amplitude observations from the four deep Kurile events. Whereas the station demeaning procedure removed much of the scatter from the travel time observations, the wide variation in slopes of the *S* to *ScS* tie lines within each data grouping indicate that much of the amplitude scatter is due to sources far from the receiver. Despite the observed scatter, however, there are subtle *S* to *ScS* trends which are worth considering.

The *sS* and *sScS* amplitude observations from events 7, 8, and 14 are shown in Figure 13*a*. As discussed above, the upgoing observations from event 16 have a strong trend which is not consistent with the observations from the other three events and were not included in this grouping. The data indicate a slight trend, with the *sScS* observations (mean value of 0.04) slightly larger than the *sS* observations (mean value of -0.04). When combined with the travel time trend of *sScS* being fast relative to *sS*, the amplitude groupings are perhaps indicative of a more attenuating structure along the *sS* paths relative to the *sScS* paths. If the arguments for a deep mantle origin of the upgoing travel time trend hold as well for amplitudes, we can isolate the attenuation structure in the deep mantle and correct the *S* and *ScS* amplitudes for its effect. However, since many of the individual *sScS* observations are in fact smaller than the corresponding *sS*

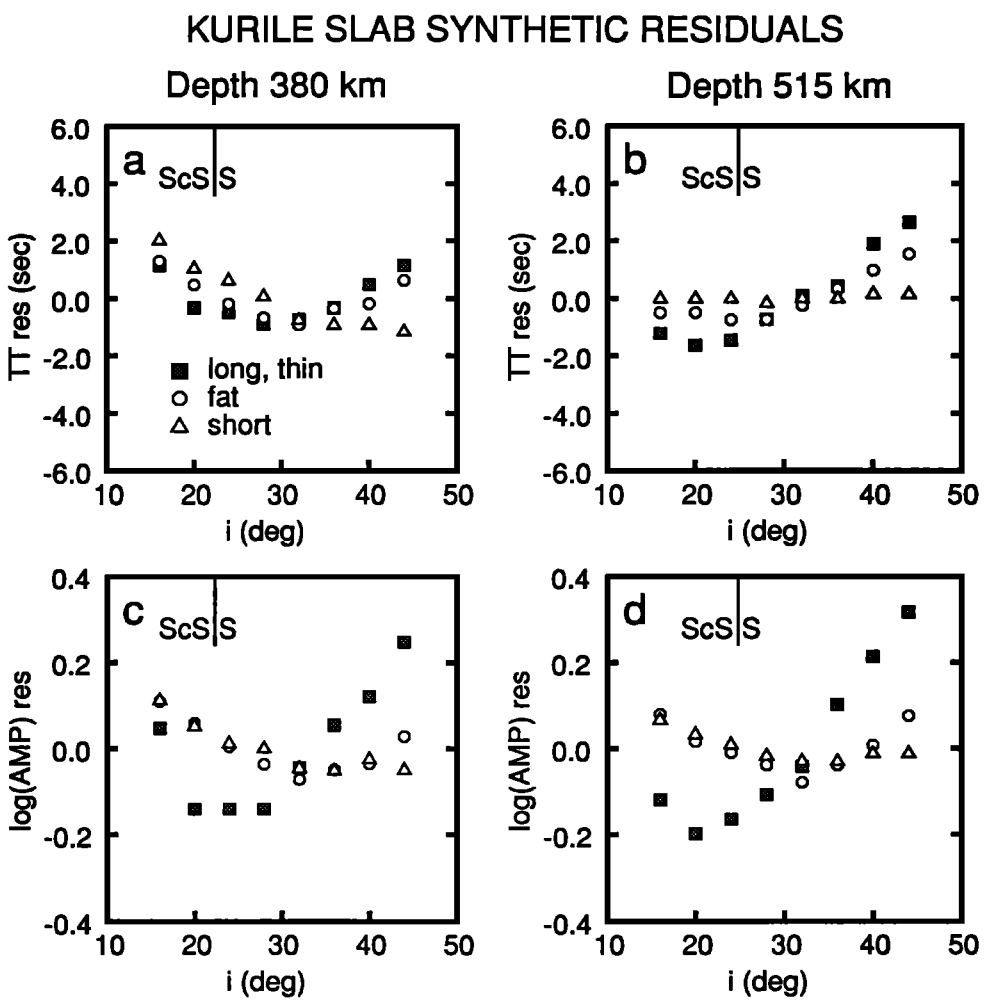

Fig. 14. Synthetic residuals versus takeoff angle for the three Kurile slab models presented in Figures 8*a*-8*c*. (*a*) Travel time residuals from 380-km source depth. (*b*) Travel time residuals from 515 km source depth. (*c*) Amplitude residuals from 380-km source depth. (*d*) Amplitude residuals from 515-km source depth. Approximate *S* and *ScS* takeoff angle ranges are indicated.

observations, the upgoing amplitude trend lacks the strong consistency of the travel time trend, and we are much less confident of this interpretation. The corrections for the lower mantle amplitude trend is fairly small (<20%) but still significant, so we explore the ramifications of pursuing this interpretation.

Figure 13*b* displays the amplitude observations from events 7 and 8. The *ScS* observations appear to be slightly small relative to *S*, the trend expected for the thin, deep slab model, although the mean values of the *S* and *ScS* residuals are less than +8% and -8% (relative to PREM), respectively, much less than that predicted for the long, thin slab. The trend of the offset for events 14 and 16 (Figure 13*c*), with *S* being smaller than *ScS*, is not consistent with the long, thin model, which predicts *ScS* defocusing even for events at source depths of 400 km (see calculated trends in Figure 9).

The amplitude residuals after the deep mantle corrections have been applied are presented in Figures 13*d* and 13*e*. Events 7 and 8 now display a stronger (±17%) offset between *S* and *ScS*, closer to that predicted for the thin, deep slab model. In contrast, the residuals for events 14 and 16 are now flat, clearly inconsistent with the strong defocusing expected for the deep, thin model. These trends will be combined with the travel time observations and compared with other slab model calculations in the next section.

Because of the sparse station distribution for the Japan slab events, the *S*-*ScS* pairing operation leaves too little data for detailed analysis. Therefore, we must rely on the patterns present in the residual rose diagrams (Figure 10) for our interpretation of deep Japan slab structure.

INTERPRETATION

By comparing the coupled travel time and amplitude behavior observed for the deep Kurile and Japan events with predictions for the suite of models presented in Figure 8, we will place constraints on the velocity structure beneath these events. Figure 14 presents the synthetic amplitude and travel time residuals for the three basic geometries hypothesized for the Kurile slab. As discussed previously, these residuals are demeaned; that is, they include only relative variations, so they can be directly compared to the downdip data residuals.

Travel Time Comparison

Figures 14*a* and 14*c* are the predictions calculated for a source depth of 380 km. It is interesting to note that at this source depth none of the slabs predict travel time residuals such that the *ScS* calculations are fast relative to *S*, as is observed in the travel time residuals that have not been corrected for the deep mantle (Figure

11*c*). This indicates that the fast *ScS* observations are indeed critically affected by deep mantle heterogeneity, and our preference for the travel time data that have been corrected for this deep mantle signal is reinforced. The corrected travel time observations (Figure 11*e*) are characterized by *S* residuals that are nearly 2 s fast relative to the *ScS* residuals. This is most consistent with the short, fast slab (*S* approximately 1.4 s fast); the long, fat slab predicts *S* observations 1 s fast relative to ScS, and the *S* residuals for the long, thin slab are only 0.7 s fast relative to *ScS*.

The travel time calculations for a source depth of 515 km are presented in Figure 14*b*. The predicted trends are smoother than those for the 380-km source because the slab extension is essentially straight below 515 km. The deep mantle corrected observations (Figure 11*d*) show *S* slightly fast (0.9 s) on average relative to *ScS*, most consistent with the short slab, which predicts no variation, or the fat slab, which predicts *ScS* to be fast by an average of only 0.2 s. If the deep mantle corrections are not applied, the data are consistent with the long, thin model, emphasizing the importance of the corrections.

Amplitude Comparison

The amplitude calculations in Figure 14*c* indicate that a 380-km-deep source in the long, thin slab will severely defocus both the *S* and *ScS* arrivals, while defocusing caused by the fat and short slabs will be less severe and will preferentially affect the *S* observations, so the *S* to *ScS* differential behavior over the limited range spanned by the data will be greater for these models than for the long, thin slab. Therefore, the uncorrected amplitude observations displayed in Figure 13*c* (*ScS* 20% larger than *S*) are very consistent with either the short or fat slabs but are slightly larger than the variation predicted for the long, thin slab (7%). If the deep mantle corrections to the amplitudes are taken into account, the observations show no *S* to *ScS* gradient in amplitude, consistent with the long, thin slab calculations by virtue of spanning a limited range of takeoff angle, but this comparison is not convincingly diagnostic.

Finally, the amplitude calculations for the 515-km-deep source are presented in Figure 14*d*. The calculations for the long, thin slab predict *S* amplitudes 40% larger than *ScS*, while the fat and short slabs predict *S* amplitudes 23% and 15% smaller than *ScS*, respectively. The defocusing of *S* relative to *ScS* in the fat and short slab models is not well correlated with the travel time calculations and seems to be controlled by the fact that the *S* energy encounters the strong lateral velocity gradients at the top edge of the slab, while the *ScS* energy exits the slab without encountering these strong gradients. While the strength of the *S* defocusing may be somewhat dependent upon our parameterization of the model structure, the relative lack of *ScS* defocusing is qualitatively robust. The amplitude observations without deep mantle corrections (Figure 13b) are characterized by *ScS* being 15% small relative to *S*. This falls between our predictions and favors a deep slab structure, but one wider or shorter than the long, thin model. The fat slab appears to be too broad, however, and the short slab too short. If the deep mantle corrections are applied to the amplitude observations (Figure 13*d*), the observed residuals are most consistent with the calculations for the long, thin model.

Interpretation of Kurile Data

A fundamental ambiguity in this analysis rests in the assessment of the deep mantle corrections. As discussed above, the consistency of the travel time behavior of the *sS* and *sScS* arrivals argues strongly for a deep mantle origin of the differential *sS* and *sScS* behavior, and the application of the resulting corrections to the *S* and *ScS* travel time data appears to be well founded. The major uncertainty is in how well the upgoing phases constrain the magnitude of the lower mantle contribution to the travel times. The amplitude behavior of the *sS* and *sScS* arrivals is not as stable, however, which argues against the application of a poorly resolved *sS* to *sScS* amplitude trend as a deep mantle correction.

In addition, we must make an effort to evaluate our relative confidence in the travel time and amplitude observations. In general, travel times have been much more extensively analyzed, and they have a relatively simple and predictable response to variations in Earth structure. This simplicity is apparent in the relative behavior between *S* and *ScS* residuals for the four Kurile events studied here. Of the 46 *S*-*ScS* pairs of residuals for these events, 42 (for the data without deep mantle corrections) display similar *S* to *ScS* differential behavior; that is, *ScS* is fast relative to *S*. This consistency elicits a high degree of confidence in the data. In contrast, the amplitude behavior of the seismic wave field is complex and poorly understood, an assessment borne out by the highly scattered differential behavior of the amplitude observations.

An argument can be made for placing high confidence in the interpretation of the amplitude observations from the deep Kurile events (events 7 and 8). In principal, the large waveform and amplitude distortions predicted for slab structure [*Vidale*, 1987; *Cormier and Kim*, 1990; *Weber*, 1990] should overwhelm the typical scatter in amplitude observations; the factor of 4 defocusing (relative to PREM) predicted by *Vidale* [1987] is in fact larger than the scatter observed here. Due to the distribution of stations and the geometry of the Kurile slab in the real Earth, actual observations only sample a limited portion of the ideal takeoff angle range that would constrain the slab structure. The predicted variation for the reduced range of takeoff angles is smaller, as is the case for the 380 km source depths in this study. However, for a 515-km or 560-km source depth, a slab dipping at an angle of 72° is well sampled by the *S* and *ScS* wavefield recorded at European stations, and thus the amplitude residuals from these events should be diagnostic of slab structure.

Therefore, if we rely primarily on the deep-mantle-corrected travel times, supported by the uncorrected amplitudes from the deepest events, we conclude that the *S* wave observations from the four deep Kurile events are inconsistent with a thin slab penetrating to great depths in the lower mantle, as proposed by *Jordan* [1977]. We cannot resolve between a short, thin slab and a longer, fat one, although the amplitude observations from events 7 and 8 do not strongly support a slab that has been thickened by a factor of 3, as modeled here. The travel times do not require a change in dip near 550 km, as proposed by *Jordan* [1977], but the amplitudes do show a small amount (15%) of systematic defocusing that is consistent with a slightly steeper dip, although this defocusing is not well predicted by any of the models examined here. The lack of evidence of a change in dip is also reported by *Suetsugu* [1989], who combines travel time tomography with forward modeling of amplitudes to argue for penetration of the Kurile slab straight into the lower mantle. Due to the small number of models that could be evaluated here, these conclusions should not be viewed as inconsistent, pending further exploration of slab geometries that will satisfy these observations.

Interpretation of Japan Data

The travel time and amplitude residual variations calculated for two source depths in the Japan slab models are presented in Figure

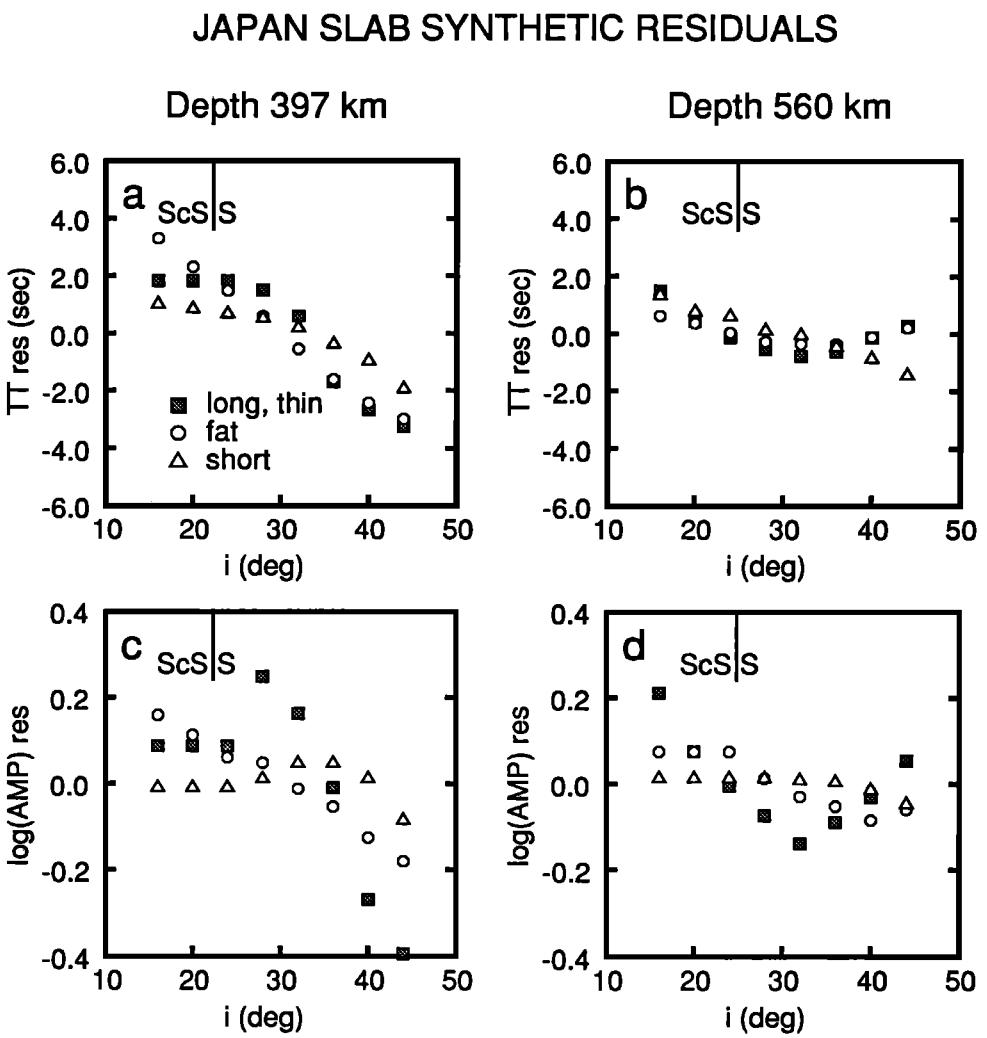

Fig. 15. Synthetic residuals vs. takeoff angle for the three Japan slab models presented in Figures 8*d*-8*e*. (*a*) Travel time residuals from 397-km source depth. (*b*) Travel time residuals from 560-km source depth. (*c*) Amplitude residuals from 397-km source depth. (*d*) Amplitude residuals from 560-km source depth. Approximate *S* and *ScS* takeoff angle ranges are indicated.

15. As discussed above, the limited data in the correct distance and azimuth range from these events makes it difficult to identify diagnostic trends; in particular, we must rely on the data as presented in Figure 10, due to the lack of *ScS* data needed for analyzing the *S-ScS* differential time patterns. We can use the predictions for the various slab models to draw some general conclusions regarding acceptable Japan slab structures given the limited data. First, note that the amplitude observations for event 6 (see Figure 10) show a strong trend, with the *S* phases with the largest takeoff angles having low amplitudes. This is consistent with defocusing in the shallow dipping slab beneath the (400 km deep) source in the upper mantle. While it was stated previously that this trend is consistent with a long, thin slab, it is now clear from Figure 15*c* that this trend is also expected for the other two slab models that we explored. Note that the deep, thin slab predicts strong focusing of the *S* arrivals near 30° takeoff angle, coinciding with the takeoff angles of several of the arrivals plotted in Figure 10. These arrivals show no sign of the expected focusing, and we tentatively conclude that a short or fat slab is more consistent with the amplitude data from this event. The scatter in the amplitude data from the two deeper events is too large to allow comparison to the strong trend calculated for the long, thin slab for these events. In addition, the calculated travel time residuals predict very similar behavior over the range of takeoff angles being examined, and therefore are not diagnostic of variation in slab structure, considering the noise level of the data.

Finally, an aspect of the data not extensively explored here is the structure of the deep mantle responsible for the strong trend in *S* to *ScS* (and *sS* to *sScS*) travel time residuals. Previous studies utilizing *ScS-S* differential times have mapped out a high-velocity zone at midlevels of the lower mantle beneath the Caribbean [*Jordan and Lynn*, 1974; *Lay*, 1983; *Grand*, 1987], a low-velocity region in the mid-lower mantle beneath Brazil [*Lay*, 1983], and low-velocity zones at the base of the mantle beneath the eastern Atlantic and India [*Lavely et al.*, 1986]. The data from events 7, 8, 14, and 16 sample the deep mantle beneath north central Siberia, and a fairly strong negative correlation found between the *S* travel time residuals and the differential times *ScS-S* (R=-0.61) may indicate the presence of an anomalously slow region at 1000-2000 km depth in the mantle. The spatial distribution of this heterogeneity and its relationship to a laterally varying discontinuity structure in *D*" is explored further by J.B. Gaherty and T. Lay [Investigation of laterally heterogeneous shear velocity structure in *D*" beneath Eurasia, submitted to *Journal of Geophysical Research*, 1991]. We do note that all recent attempts to develop empirical receiver and deep mantle corrections for *P* waves [*Grand and Ding*, 1989; *Suetsugu*, 1989; *Zhou and Anderson*, 1989; *Zhou et al.*, 1990] are coming to the compatible

conclusion that much of the power in the residual sphere travel time patterns is in fact caused by deep mantle structure.

CONCLUSIONS

We place further constraints on the deep velocity structure of the Kurile and Japan slabs by analyzing a large data set consisting of *S* wave travel time and amplitude residuals from deep focus earthquakes. We have empirically evaluated the systematic patterns present in the data due to heterogeneous lower mantle structure and compare the corrected observations with synthetic residuals calculated for models based on the deep slab structures proposed by *Creager and Jordan* [1984, 1986] and *Fischer et al.* [1988]. We find the following:

1. *sS* and *sScS* travel time residuals indicate that there is a large-scale velocity heterogeneity in the lower mantle beneath northern Siberia that fortuitously imitates a slab-like signature in the *S* and *ScS* travel time observations from deep Kurile events recorded at European WWSSN stations. Once this pattern is removed, the resulting travel time residuals are not compatible with the steeply dipping slab structure preferred by *Jordan* [1977]. Furthermore, although we hesitate to claim that the presence of a lower mantle shear velocity structure implies a similar *P* velocity structure, we point out that possibility that the *P* wave residual spheres are also biased by such a structure. *Creager and Jordan* [1984] note that the travel time residual versus takeoff angle gradient that we have investigated in detail here is in fact stronger for the *P* wave residual spheres from the deepest Kurile events than for the *S* wave residual sphere investigated by *Jordan* [1977], so it seems reasonable that similar deep mantle structure could be responsible for both patterns. *Zhou and Anderson* [1989], *Grand and Ding* [1989], and *Zhou et al.* [1990] have argued that other portions of the *P* wave residual sphere patterns are dominated by lower mantle and receiver structure in other regions. Overall, it seems clear that both the *P* and *S* lower mantle structure must be well determined before the travel time residual spheres can be unambiguously interpreted in terms of near-source structure.

2. Once lower mantle corrections are applied to the travel time residuals from the deep Kurile events, a substantially shorter and/or broader slab than that preferred by *Creager and Jordan* [1984, 1986] appears to be most consistent with the *S* wave travel time and amplitude observations in the downdip direction. Slabs with extreme broadening also appear to be inconsistent with the observations, limiting the extent of deformation of the slab near the 670-km discontinuity to less than a factor of 3 thickening.

Differentiating between a slab that terminates near 670-km and one that broadens and penetrates into the lower mantle is very difficult using data constrained to the downdip direction. However, this analysis, which emphasizes differential behavior between similar phases, eliminates many of the unknown quantities that complicate interpretations of azimuthal patterns in travel times and amplitudes (i.e., location errors, deep mantle structure, rapid station variations). This increases our confidence that we are, in fact, isolating and modeling the near-source structure. Down-dip sampling at a larger range of takeoff angles than that provided by European WWSSN stations would remove much of the ambiguity from the analysis. Alternatively, a dense network providing broadband data with full three-dimensional coverage would allow a more detailed evaluation of slab diffraction waveform effects beyond those manifested in simple travel time and amplitude observations.

Acknowledgments. J.B.G. received a Turner Fund grant from the Department of Geological Sciences at the University of Michigan. Special thanks to C. Young for the North American data used in this analysis, a thorough review of the manuscript, and many helpful discussions. K. Toy provided a tabulation of his travel time station statics; J. Edwards assisted with the digitizing; M. Weber, V. Cormier, and an anonymous reviewer provided helpful reviews of the manuscript. J.B.G. thanks T. Jordan for financial support, and B. Hager and T. Herring for computer time, during completion of this work at MIT. This research was supported by grants EAR 8451715 (T.L.) and EAR 8707578 (J.E.V.) from the National Science Foundation and by the W.M. Keck Foundation. Contribution 112, Institute of Tectonics and C.F. Richter Seismological Laboratory, U.C. Santa Cruz.

REFERENCES

Agnon, A., and M.S.T. Bukowinski, ∂s at high pressure and *d*ln*Vs*/*d*ln*Vp* in the lower mantle, *Geophys. Res. Lett.*, *17*, 1149-1152, 1990.

Aki, K., and P.G. Richards, *Quantitative Seismology*, 932 pp., W.H. Freeman, New York, 1980.

Anderson, D.L., Thermally induced phase changes, lateral heterogeneity of the mantle, continental roots and deep slab anomalies, *J. Geophys. Res.*, *92*, 13,968-13,980, 1987*a*.

Anderson, D.L., A seismic equation of state, II, Shear properties and thermodynamics of the lower mantle, *Phys. Earth Planet. Inter.*, *45*, 307-323, 1987*b*.

Apperson, K.D., and C. Frohlich, The relationship between Wadati-Benioff zone geometry and *P*, *T*, and *B* axes of intermediate and deep focus earthquakes, *J. Geophys. Res.*, *92*, 13,821-13,831, 1987.

Baumgardt, D.R., Evidence for a *P*-wave velocity anomaly in *D"*, *Geophys. Res. Lett.*, *16*, 657-660, 1989.

Beck, S.L., and T. Lay, Test of the lower mantle slab penetration hypothesis using broadband *S* waves, *Geophys. Res. Lett.*, *13*, 1007-1010, 1986.

Butler, R., and L.J. Ruff, Teleseismic short-period amplitudes: Source and receiver variations, *Bull. Seismol. Soc. Am.*, *70*, 831-850, 1980.

Cormier, V.F., Slab diffraction of *S* waves, *J. Geophys. Res.*, *94*, 3006-3024, 1989.

Cormier, V.F., and W. Kim, Three-dimensional modeling of subducted lithospheric slabs from the amplitudes and waveforms of *S* waves, *Sci. Rep. 2*, pp. 9-52, Geophys. Lab., Hanscom Air Force Base, Mass., 1990.

Creager, K.C., and T.H. Jordan, Slab penetration into the lower mantle, *J. Geophys. Res.*, *89*, 3031-3049, 1984.

Creager, K.C., and T.H. Jordan, Slab penetration into the lower mantle beneath the Mariana and other island arcs of the northwest Pacific, *J. Geophys. Res.*, *91*, 3573-3589, 1986.

Davies, D., and D.P. McKenzie, Seismic travel-time residuals and plates, *Geophys. J. R. Astron. Soc.*, *18*, 51-63, 1969.

Dziewonski, A.M., Mapping the lower mantle: Determination of lateral heterogeneity in *P* velocity up to degree and order 6, *J. Geophys. Res.*, *89*, 5929-5952, 1984.

Dziewonski, A.M., and D.L. Anderson, Preliminary reference earth model, *Phys. Earth Planet. Inter.*, *25*, 297-356, 1981.

Dziewonski, A.M., and D.L Anderson, Travel times and station corrections for *P* waves at teleseismic distances, *J. Geophys. Res.*, *88*, 3295-3314, 1983.

Engdahl, E.R., and D. Gubbins, Simultaneous travel time inversion for earthquake locations and subduction zone structure in the central Aluetian Islands, *J. Geophys. Res.*, *92*, 13,855-13,862, 1987.

Fischer, K.M., T.H. Jordan, and K.C. Creager, Seismic constraints on the morphology of deep slabs, *J. Geophys. Res.*, *93*, 4773-4783, 1988.

Fischer, K.M., K.C. Creager, and T.H. Jordan, Mapping the Tonga slab, *J. Geophys. Res., in press*, 1991.

Fitch, T.J., Compressional velocity in source regions of deep earthquakes, *Earth Planet. Sci. Lett.*, *26*, 156-166, 1975.

Frohlich, C., The nature of deep focus earthquakes, *Annu. Rev. Earth Planet. Sci.*, *17*, 227-254, 1989.

Giardini, D., and J.H. Woodhouse, Deep seismicity and modes of deformation in Tonga subduction zone, *Nature*, *307*, 505-509, 1984.

Grand, S.P., Tomographic inversion for shear velocity structure beneath the North American Plate, *J. Geophys. Res.*, *92*, 14,065-14,090, 1987.

Grand, S.P., A possible station bias in travel time measurements reported to ISC, *Geophys. Res. Lett.*, *17*, 17-20, 1990.

Grand, S.P., and X.-Y. Ding, Residual spheres and slab penetration into the lower mantle (abstract), *Eos Trans. AGU*, *70*, 1322, 1989.

Gurnis, M., and B.H. Hager, Controls on the structure of subducted slabs, *Nature, 335*, 317-321, 1988.

Isacks, B., and P. Molnar, Distribution of stresses in the descending lithospere from a global survey of focal-mechanism solutions of mantle earthquakes, *Rev. Geophys., 9*, 103-172, 1971.

Isacks, B., J. Oliver, and L.R. Sykes, Seismology and the new global tectonics, *J. Geophys. Res., 73*, 5855-5899, 1968.

Jeanloz, R., and E. Knittle, Density and composition of the lower mantle, *Philos. Trans. R. Soc. London, Ser. A, 328*, 377-389, 1989.

Jordan, T.H., Lithospheric slab penetration into the lower mantle beneath the Sea of Okhotsk, *J. Geophys., 43*, 473-496, 1977.

Jordan, T.H., and W.S. Lynn, A velocity anomaly in the lower mantle, *J. Geophys. Res., 79*, 2679-2685, 1974.

Kamiya, S., T. Miyatake, and K. Hirahara, How deep can we see the high velocity anomalies beneath the Japan Islands?, *Geophys. Res. Lett., 15*, 828-831, 1988.

Kamiya, S., T. Miyatake, and K. Hirahara, Three dimensional P wave velocity structure beneath the Japanese Islands, *Bull. Earthquake. Res. Inst. Univ. Tokyo, 64*, 457-485, 1989.

Lavely, E.M., D.W. Forsyth, and P. Friedemann, Scales of heterogeneity near the core-mantle-boundary, *Geophys. Res. Lett., 13*, 1505-1508, 1986.

Lay, T., Localized velocity anomalies in the lower mantle, *Geophys. J. R. Astron. Soc., 72*, 483-516, 1983.

Lay, T., and D.V. Helmberger, Body wave amplitude and travel time correlations across North America, *Bull. Seismol. Soc. Am., 73*, 1063-1076, 1983*a*.

Lay, T., and D.V. Helmberger, A lower mantle S wave triplication and the shear velocity structure of *D"*, *Geophys. J. R. Astron. Soc., 75*, 799-838, 1983*b*.

Mikumo, T., Source process of deep and intermediate earthquakes as inferred from long-period *P* and *S* waveforms, 2. Deep focus and intermediate depth earthquakes around Japan, *J. Phys. Earth, 19*, 303-320, 1971.

Rees, B.A., and E.A. Okal, The depth of the deepest historical earthquakes, *Pure Appl. Geophys., 125*, 699-715, 1987.

Ribe, N.M., Seismic anisotropy and mantle flow, *J. Geophys. Res., 94*, 4213-4223, 1989.

Romanowicz, B.A., and M. Cara, Reconsideration of the relations between *S* and *P* station anomalies in North America, *Geophys. Res. Lett., 7*, 417-420, 1980.

Schwartz, S.Y., T. Lay, and S.L. Beck, Shear wave travel time, amplitude, and waveform analysis: Constraints on deep slab structure and mantle heterogeneity, for earthquakes in the Kurile slab, *J. Geophys. Res., in press*, 1991.

Sengupta, M.K., The structure of the Earth's mantle from body wave observations, Sc.D. thesis, 578 pp., Mass. Inst. of Technol., Cambridge, 1975.

Silver, P.G., and W.W. Chan, Observations of body wave multipathing from broadband seismograms: Evidence for lower mantle slab penetration beneath the Sea of Okhotsk, *J. Geophys. Res., 91*, 13,787-13,802, 1986.

Silver, P.G., R.W. Carlson, and P. Olson, Deep slabs, geochemical heterogeneity, and large-scale structure of mantle convection: Investigation of an enduring paradox, *Annu. Rev. Earth Planet. Sci., 16*, 477-541, 1988.

Spakman, W., S. Stein, R. van der Hilst, and R. Wortel, Resolution experiments for NE Pacific subduction zone tomography, *Geophys. Res. Lett., 16*, 1097-1100, 1989.

Stark, P.B., and C. Frohlich, The depths of the deepest deep earthquakes, *J. Geophys. Res., 90*, 1859-1869, 1985.

Stead, R.J., and D.V. Helmberger, Numerical-analytical interfacing in two dimensions with applications to modeling NTS seismograms, *Pure Appl. Geophys., 128*, 157-193, 1988.

Strelitz, R., The September 5, 1970 Sea of Okhotsk earthquake: A multiple event with evidence of triggering, *Geophys. Res. Lett., 2*, 124-127, 1975.

Suetsugu, D., Lower mantle high velocity zone beneath the Kurils as inferred from *P* wave travel time and amplitude data, *J. Phys. Earth, 37*, 265-295, 1989.

Tanimoto, T., Long-wavelength *S*-wave velocity structure throughout the mantle, *Geophys. J. Int., 100*, 327-336, 1990.

Toy, K.M., Tomographic analysis of ISC travel time data for earth structure, Ph.D. thesis, Univ of Calif, San Diego, 1989.

Vassiliou, M.S., The state of stress in subducting slabs as revealed by earthquakes analyzed by moment tensor inversion, *Earth Planet. Sci. Lett., 69*, 195-202, 1984.

Veith, K.F. The relationship of island arc seismicity to plate tectonics, Ph.D. thesis, South. Methodist Univ., Dallas, Tex, 1974.

Vidale, J.E., Waveform effects of a high velocity, subducted slab, *Geophys. Res. Lett., 14*, 542-545, 1987.

Weber, M., Subduction zones--Their influence on traveltimes and amplitudes of *P* waves, *Geophys. J. Int., 101*, 529-544, 1990.

Weber, M., and J.P. Davis, Evidence of a laterally inhomogeneous lower mantle structure from *P*- and *S*-waves, *Geophys. J. Inter., 102*, 231-255, 1990.

Wickens, A.J., and G.G.R. Buchbinder, *S*-wave residuals in Canada, *Bull. Seismol. Soc. Am., 70*, 809-822, 1980.

Witte, D., The pseudospectral method for simulating wave propagation, Ph.D. thesis, Columbia Univ., New York, 1989.

Zhou, H.-W., How well can we resolve the deep seismic slab with seismic tomography?, *Geophys. Res. Lett, 15*, 1425-1428, 1988.

Zhou, H.-W., and D.L. Anderson, Teleseismic contributions to focal residual spheres and Tangshen earthquake sequence (abstract), *Eos Trans. AGU, 70*, 1322, 1989.

Zhou, H.-W., and R.W. Clayton, *P* and *S* wave travel time inversions for subducting slabs under the island arcs of the northwest Pacific, *J. Geophys. Res., 95*, 6829-6851, 1990.

Zhou, H.-W., D.L. Anderson, and R.W. Clayton, Modeling of residual spheres for subduction zone earthquakes, 1., Apparent slab penetration signatures in the NW Pacific caused by deep diffuse mantle anomalies, *J. Geophys. Res., 95*, 6799-6827, 1990.

J.B. Gaherty, Rm. 54-526, Department of Earth, Atmospheric, and Planetary Sciences, Massachusetts Institute of Technology, Cambridge, MA 02139.

T. Lay, Institute of Tectonics, Earth Sciences Board, Applied Sciences Bldg., University of California, Santa Cruz, CA 95060.

J.E. Vidale, U.S. Geological Survey, 345 Middlefield Road, MS 977, Menlo Park, CA 94025.

(Received October 19, 1990;
revised March 4, 1991;
accepted May 28, 1991.)